ACS Partner Journal

PHOTON SCIENCE

pubs.acs.org/photonsci

Article

The Gotthard-II Charge-Integrating Silicon Microstrip Detector for the FEL and Synchrotron Applications

Jiaguo Zhang,* Anna Bergamaschi, Martin Brückner, Maria Carulla, Roberto Dinapoli, Simon Ebner, Khalil Daniel Ferjaoui, Erik Fröjdh, Viveka Gautam, Dominic Greiffenberg, Vadym Kedych, Dmitry Khakhulin, Shqipe Hasanaj, Julian Heymes, Viktoria Hinger, Thomas King, Shuqi Li, Carlos Lopez-Cuenca, Alice Francesca Mazzoleni, Davide Mezza, Konstantinos Moustakas, Martin Müller, Jonathan Franklin Mulvey, Aldo Mozzanica, Kirsty Anne Paton, Marco Ramilli, Christian Ruder, Patrick Sieberer, Saverio Silletta, Bernd Schmitt, Grigory Smolentsev, Dhanya Thattil, Monica Turcato, Xiangyu Xie, and Hazem Yousef

Cite This: https://doi.org/10.1021/photonsci.5c00027

Read Online

ACCESS | Metrics & More | Article Recommendations

ABSTRACT: Gotthard-II is a charge-integrating silicon microstrip detector developed for energy-dispersive experiments and X-ray photon beam diagnostics at the European X-ray Free-Electron Laser (EuXFEL). Its one-dimensional geometry, featuring fewer readout channels than pixel detectors, and its fast readout capability make it the only segmented detector able to perform experiments at a 4.5 MHz frame rate while capturing all 2700 X-ray pulses in a bunch train produced by the EuXFEL machine. The Gotthard-II detector was tested for single-photon sensitivity and dynamic range, meeting all specifications. In addition to FEL applications operating at a 4.5 MHz frame rate in burst mode, the detector supports continuous acquisition at up to 400 kHz and counting mode at ≤4.5 MHz for synchrotron applications. Experimental tests with standard samples using X-ray diffraction and X-ray emission spectroscopy were conducted at several beamlines of the Swiss Light Source (SLS) and EuXFEL. The measurement results were compared with those obtained using established detectors at these beamlines, demonstrating the performance of the detector in energy-dispersive experiments.

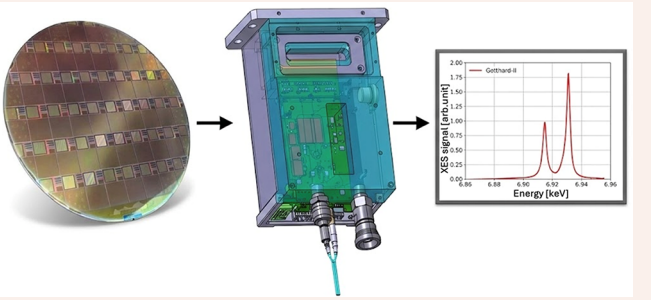

KEYWORDS: *Gotthard-II, high frame-rate detector, FEL, synchrotron radiation detector, 1D detector, FEL and synchrotron applications*

1. INTRODUCTION

Free-Electron Lasers (FELs) deliver ultrashort (<100 fs), high-intensity (10^{12} photons/pulse), and fully coherent X-ray pulses with a peak brilliance ~8 orders of magnitude higher than any synchrotron radiation source. The femtosecond X-ray pulses are capable of unlocking challenging research opportunities through single-bunch timing experiments, for example, studying ultrafast molecular and atomic dynamic processes. Among all FELs available in the world, the European X-ray Free-Electron Laser (EuXFEL) in Schenefeld[1] is unique due to its bunch structure: the bunch spacing is 220 ns between the 2700 pulses in a train, and the repetition rate of the bunch train is 10 Hz with an inter-train interval of 99.4 ms. It poses significant challenges to pixel detectors, in particular the 4.5 MHz frame rate, which requires local storage of images in the detector since it is unfeasible to read out images during the 220 ns bunch spacing.

At present, a few pixel detectors, for example, the Adaptive Gain Integrating Pixel Detector (AGIPD),[2] the Large Pixel Detector (LPD),[3] the detector based on DEPFET Sensor with Signal Compression (DSSC),[4] as well as the JUNGFRAU detector,[5] have been commissioned at several beamlines and are available for user experiments at the EuXFEL. Most of these detectors have demonstrated performance in user experiments since the start of their operation, resulting in high-impact research outcomes.[6,7] However, these detectors are unable to fully utilize the 2700 pulses of the EuXFEL due to the limited pixel size and the resulting difficulty of integrating a complete storage circuit into the readout ASIC with a memory depth sufficient to store all images generated by

Received: September 8, 2025
Revised: December 17, 2025
Accepted: December 17, 2025

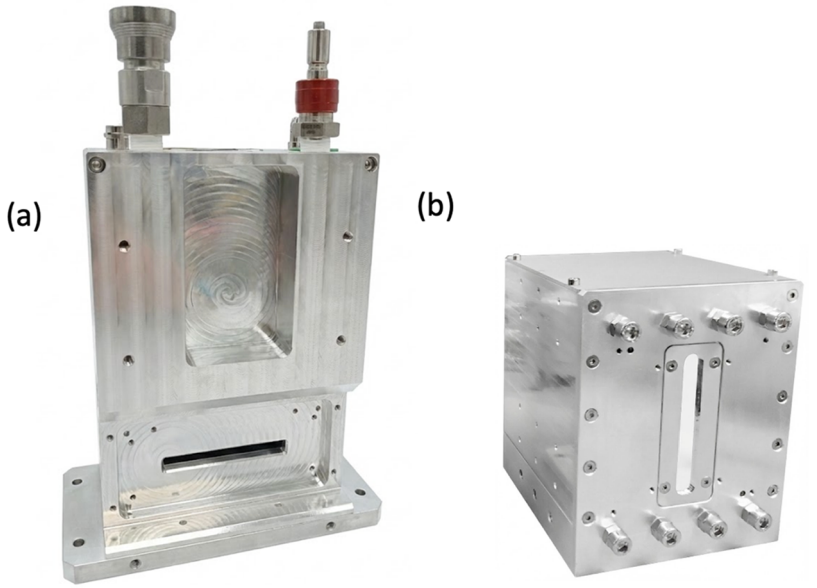

Figure 1. Two versions of the Gotthard-II detector: (a) 50 μm pitch with 1280 strip channels, and (b) 25 μm pitch with 2560 strip channels.

the X-ray bunches in a train. As a result, only a fraction of the XFEL pulses are captured by the pixel detectors, depending on the available memory depth of each detector.

The Gotthard-II is a silicon microstrip detector with a pitch of either 50 μm or 25 μm, and features 1280 or 2560 channels. It is expected to become the most widely used detector for energy-dispersive experiments at the EuXFEL, which are particularly suited for one-dimensional detectors. Unlike pixel detectors, the readout ASIC of Gotthard-II is not constrained in the second dimension. This allows for the integration of compact digital storage with a memory depth of 2700, enabling acquisition at a 4.5 MHz frame rate for all pulses in an EuXFEL bunch train. As a result, Gotthard-II is the only detector capable of fully utilizing the unique pulse characteristics of the EuXFEL machine. Used as a diagnostic tool, Gotthard-II is also capable of generating a veto pattern based on its detection of the incoming pulses. Such information can be used, for example, to optimize the memory usage of large-area megahertz pixel detectors by indicating which images to store in memory.

In addition to the aforementioned burst operation utilizing on-chip digital storage, it is possible to use the Gotthard-II detector in two additional operation modes: continuous operation mode up to 400 kHz and photon counting mode at a rate below 4.5 MHz using each channel's digital comparator to count photon hits above a certain threshold. This versatility makes it possible to employ the detector for experiments at other synchrotron radiation sources and enhances its applicability to FELs operating in continuous wave (CW) mode.

In this paper, we introduce the design of the Gotthard-II detector, present its three operation modes (burst, continuous, and counting), and discuss its calibration procedures and performance along with the temperature dependence of calibration constants. Furthermore, experimental tests were conducted at several beamlines at the Swiss Light Source (SLS, synchrotron) and the EuXFEL, including X-ray diffraction (XRD) and X-ray emission spectroscopy (XES). The results are compared to those obtained using well-established detectors for user experiments at these beamlines to validate the performance of Gotthard-II. Under identical experimental conditions, the Gotthard-II detector achieves comparable data quality.

2. EXPERIMENTAL MATERIAL: DESIGN OF THE GOTTHARD-II DETECTOR

The Gotthard-II detector has fewer readout channels but exhibits similar complexity compared to other pixel detectors at the EuXFEL. To support proper scientific experiments, Gotthard-II must achieve a frame rate up to 4.5 MHz, a dynamic range of up to 10^5 keV, and single-photon resolution for photon energies in the 5.4 keV to 25 keV range.

The Gotthard-II detector comes in two designs: one with a 50 μm pitch and 1280 channels, and another with a 25 μm pitch and 2560 channels. Both detector designs employ the same ASICs, which feature input pads with a 50 μm pitch. The 25 μm detector pitch is achieved by interleaving the strips to ASICs on opposite sides. The finer 25 μm pitch is intended for experiments requiring higher spatial resolution, such as with the High-REsolution hard X-ray single-shot spectrometer (HiREX).[8] The 50 μm pitch detector has a detection area of 512 mm^2 with a 64 mm coverage in the spatial resolution direction, while the 25 μm pitch detector has a detection area of 384 mm^2 with the same coverage in the spatial resolution direction. The designs of the 50 and 25 μm pitch Gotthard-II detectors are shown in Figure 1.

The Gotthard-II detectors require liquid cooling to effectively dissipate the heat generated by the electronics and the readout board. The power consumption is approximately 12.5 W for the 50 μm pitch detector and 25 W for the 25 μm pitch detector. Both are powered by a +12 V supply.

The primary components of the Gotthard-II detector include the front-end module (ASIC, sensor, and high-density interconnect), the readout board, and the control/data interfaces.

2.1. Hardware and Specifications. *2.1.1. ASIC.* The development of the Gotthard-II readout ASIC began in 2015. The complete history of the ASIC's development is depicted in Figure 2. It includes five analog front-end prototypes (G-1.4/

https://doi.org/10.1021/photonsci.5c00027
Photon Sci. XXXX, XXX, XXX−XXX

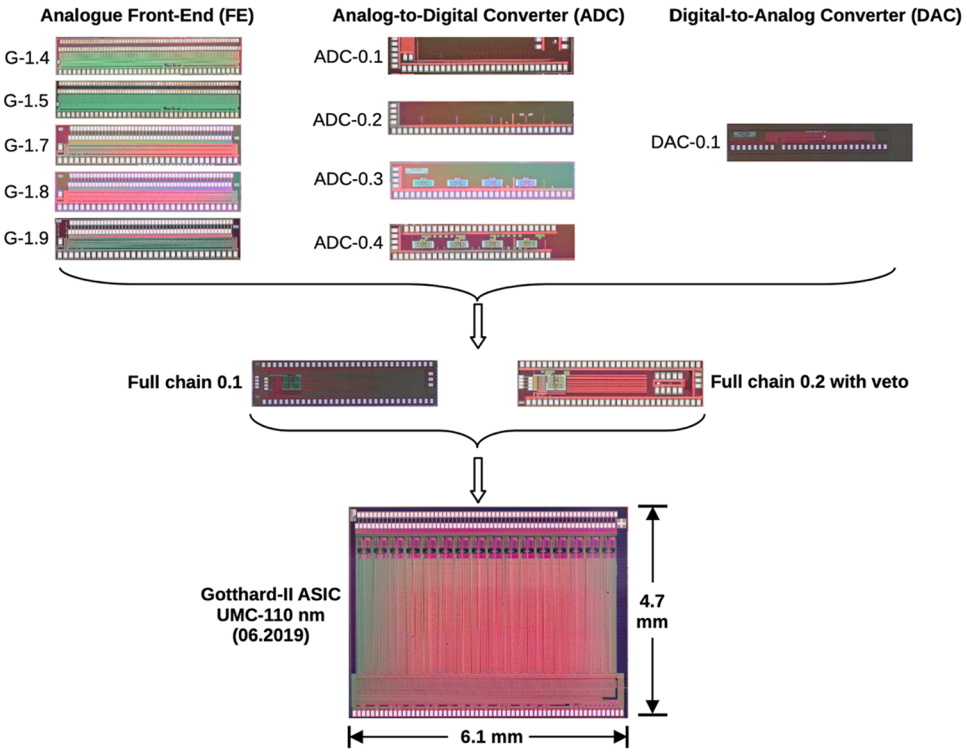

Figure 2. A history review of the Gotthard-II readout ASIC development. The full size of the Gotthard-II ASIC was fabricated using UMC-110 nm technology, with a size of 4.7 mm × 6.1 mm.

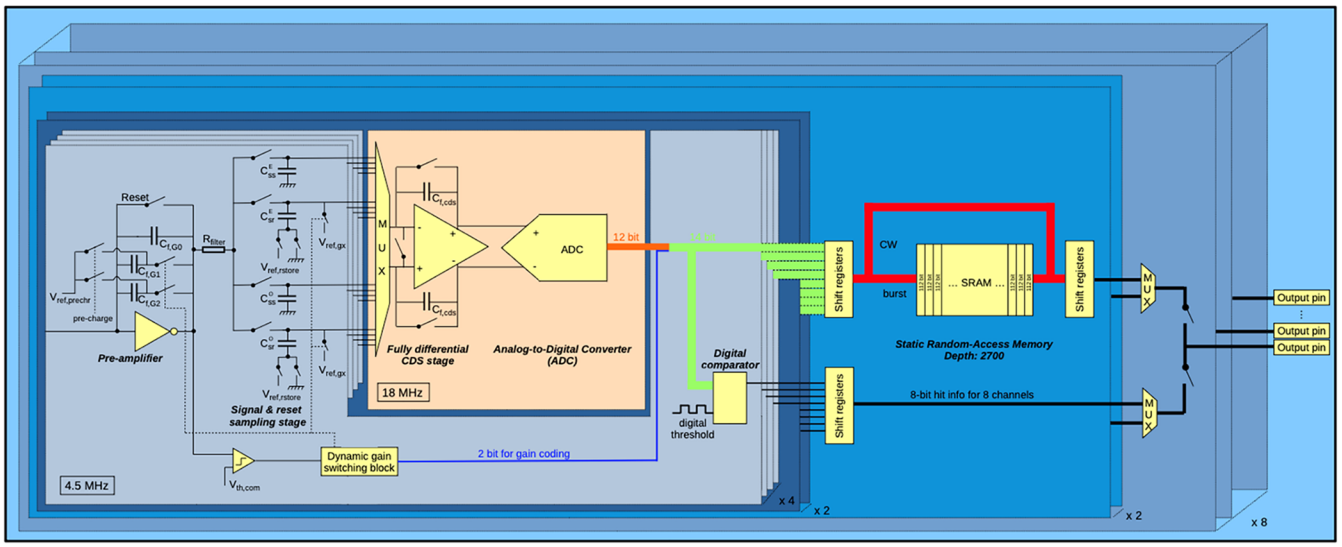

Figure 3. Circuit diagram of the Gotthard-II readout ASIC. $C_{f,G0}$, $C_{f,G1}$ and $C_{f,G2}$ are the three feedback capacitors of the dynamic gain switching pre-amplifier. The photo is reproduced from Zhang et al., 2021.[11]

1.5/1.7/1.8/1.9) aimed at optimizing noise, DC gain, and speed. For signal readout, single-ended and differential outputs were used in these prototypes. Additionally, four successive approximation register (SAR) analog-to-digital converter (ADC) prototypes (ADC-0.1/0.2/0.3/0.4, 12 bits) were designed with various capacitor array architectures to minimize total capacitance, thereby improving the sampling and conversion rates. These prototypes also incorporated different configurable delays before each comparison and parasitic capacitance to enhance output linearity.[9,10] One digital-to-analog converter prototype (DAC-0.1, 10 bits) was developed to supply the on-chip bias. Two full-chain prototypes (Full chain 0.1/0.2) with eight readout channels were designed, incorporating all the aforementioned components, as well as an additional compact digital storage with a memory depth of 2720 for all EuXFEL pulses and a digital comparator for each strip channel for generating veto signals. These prototypes were used to validate the functionality after assembling all individual components.

Based on the optimized designs of each component from the prototypes, the full-size Gotthard-II ASIC,[11] featuring 128 readout channels per chip, was fabricated in mid-2019 using UMC-110 nm technology.

https://doi.org/10.1021/photonsci.5c00027
Photon Sci. XXXX, XXX, XXX−XXX

Table 1. Specifications of the 50 and 25 μm Pitch Gotthard-II Detector[a]

Parameter	Value	Unit and remark
Energy range	5.4* - 25	keV
Pitch of strip	50 | 25	μm
Sensor thickness	450 | 320	μm
Quantum efficiency	83.5% | 72.2%	@ 12.4 keV (calculation)
Sensitive area	64 x 8 | 64 x 6	mm^2
Number of strips	1280 | 2560	
Sensor material	silicon	
Dynamic range	$> 10^5$	keV
Linearity	better than 1% non-linearity	
ADC resolution	10	bit
Point spread function	O(pitch)	
Integration time	≥ 100	ns
Noise	< 300	e^- r.m.s.
Signal-to-noise ratio (SNR)	> 10	@ 12.4 keV
Single-photon detection	≥ 5.4	keV with SNR ≥ 5
Frame rate in burst mode	4.5	MHz
Readout time in burst mode	< 6	ms for 2700 frames in a burst
Readout latency of veto signal**	< 500	ns
Frame rate in continuous mode	400	kHz
Readout time in continuous mode	< 2.5	μs
Frame rate in counting mode	4.5	MHz
Readout time in counting mode	< 165	ns
Vacuum compatibility	10^{-4} - 10^{-5}	mbar
Cooling	liquid	

[a]Blue: unique specifications for 50 μm pitch detector. Red: unique specifications for 25 μm pitch detector. * Minimal photon energy with single-photon resolution. ** Pulse to end of transmission @ optical fiber.

Figure 3 shows the circuit diagram of the Gotthard-II readout ASIC. It features: (a) a high-speed, three-fold dynamic gain-switching pre-amplifier (PRE) designed to work at the required 4.5 MHz frame rate. The dynamic gain-switching circuit enables the detection of integrated photon energies up to 10^5 keV while maintaining single-photon resolution with a signal-to-noise ratio (SNR) greater than 10 for 12.4 keV photons with low photon fluxes (Table 1). The three gains over the entire dynamic range are noted as G0, G1, and G2 (from high to low). The output of the PRE can be connected to two sets of analog storage capacitors (for storing data from frames with "even" or "odd" index respectively) through a configurable filtering resistor R_{filter} to remove the high frequency noise; (b) a correlated-double-sampling (CDS) stage to remove the low frequency noise and to provide additional amplification of the signal at the output of the PRE with a factor of 2.2 or 3; (c) an on-chip analog-to-digital converter (ADC) with 12-bit output; (d) a static random-access memory (SRAM) capable of storing all digitized images from the 2700 pulses in a bunch train; and (e) an on-chip digital comparator for each channel to generate veto signals for pixel detectors.

A 14-bit threshold can be set for the digital comparator of each channel: The 12-bit output from the ADC, together with 2 bits at the most significant bit (MSB) for coding the gain used by the dynamic gain switching PRE, will be compared to the given threshold input. If the 14-bit output of the channel is above the threshold, the digital comparator outputs "1," and thus a photon hit is measured and saved in a register. The sum of photon hits of all strip channels is low if the interaction

https://doi.org/10.1021/photonsci.5c00027
Photon Sci. XXXX, XXX, XXX−XXX

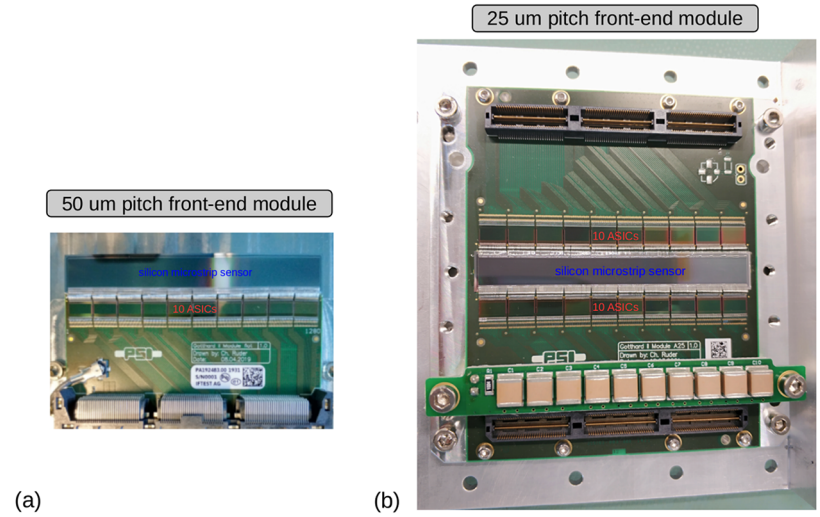

Figure 4. Gotthard-II front-end modules: (a) 50 μm pitch, and (b) 25 μm pitch version.

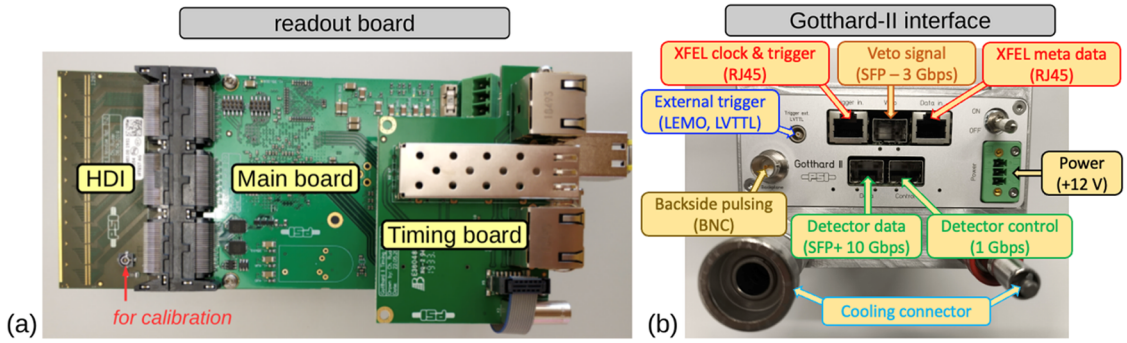

Figure 5. (a) Readout board, and (b) interface of Gotthard-II.

between the X-ray pulse and the sample during user experiments is poor or the X-ray pulse is unqualified, which forms the basis of vetoing. These veto signals allow the selected memory locations of pixel detectors, storing empty images caused by poor interactions or unqualified X-ray pulses, to be reused for forthcoming pulses during the same bunch train. Further details about the Gotthard-II ASIC design and performance can be found in Zhang et al., 2021.[11]

The default operation mode of the Gotthard-II readout ASIC is burst mode at a 4.5 MHz frame rate for the EuXFEL. Additionally, a continuous operation mode has been implemented for synchrotron experiments and FELs operating in continuous wave (CW) mode. During the veto signal generation, thanks to the output of the digital comparator, photon-counting mode with 1-bit output becomes possible. The different operation modes will be discussed in Section 2.3.

2.1.2. Sensor. The silicon sensor used in the front-end module is fabricated on an n-type silicon substrate with segmented p-electrodes serving as the strip readout. Holes generated by incident X-ray photons are collected by these readout electrodes. It has a pitch of either 50 μm or 25 μm. The sensor thicknesses are 450 and 320 μm for the 50 and 25 μm pitch, respectively, resulting in quantum efficiencies of 83.5 and 72.2% for 12.4 keV X-ray photons from theoretical calculations. The strip lengths are 8 and 6 mm long for the 50 and 25 μm pitch, respectively. The reduction in strip length for the 25 μm pitch sensor helps minimize the capacitive coupling effect between neighboring strip channels.[9]

All strips are surrounded by a current-collection ring (CCR) biased to the ground, which collects the current generated at the sensor periphery and ensures a more uniform electric field distribution near the border of the strip region. A floating guard ring is also implemented to prevent early sensor breakdown. The entire periphery covers a 1 mm-wide region surrounding all strips, which is insensitive to X-rays.

The sensors are fabricated by Hamamatsu Photonics.[12] All produced sensors have been tested and have demonstrated a breakdown voltage of >200 V, which is well above the nominal operating voltage of the Gotthard-II sensor and the full depletion voltage (typically between 60 and 90 V, depending on doping concentration and sensor thickness).

2.1.3. High-Density Interconnect. The silicon sensor and readout ASICs are glued onto the high-density interconnect (HDI) printed circuit board (PCB), which itself is glued onto an aluminum frame. Each strip of the silicon sensor is wire-bonded to an input channel of the readout ASIC. The input-outputs (IOs) of the ASICs (60 IOs per ASIC) are also wire-bonded to the HDI. These IOs include control signals for the logic within the ASIC, bias supply, clocks, and data output. To ensure stable voltages with minimal noise, buffers and RC filters are implemented on the HDI.

The HDI features either one or two 128-pin connectors: one for the 50 μm pitch detector, and two for the 25 μm pitch detector. The HDI is connected to the readout board via the 128-pin connector.

https://doi.org/10.1021/photonsci.5c00027
Photon Sci. XXXX, XXX, XXX−XXX

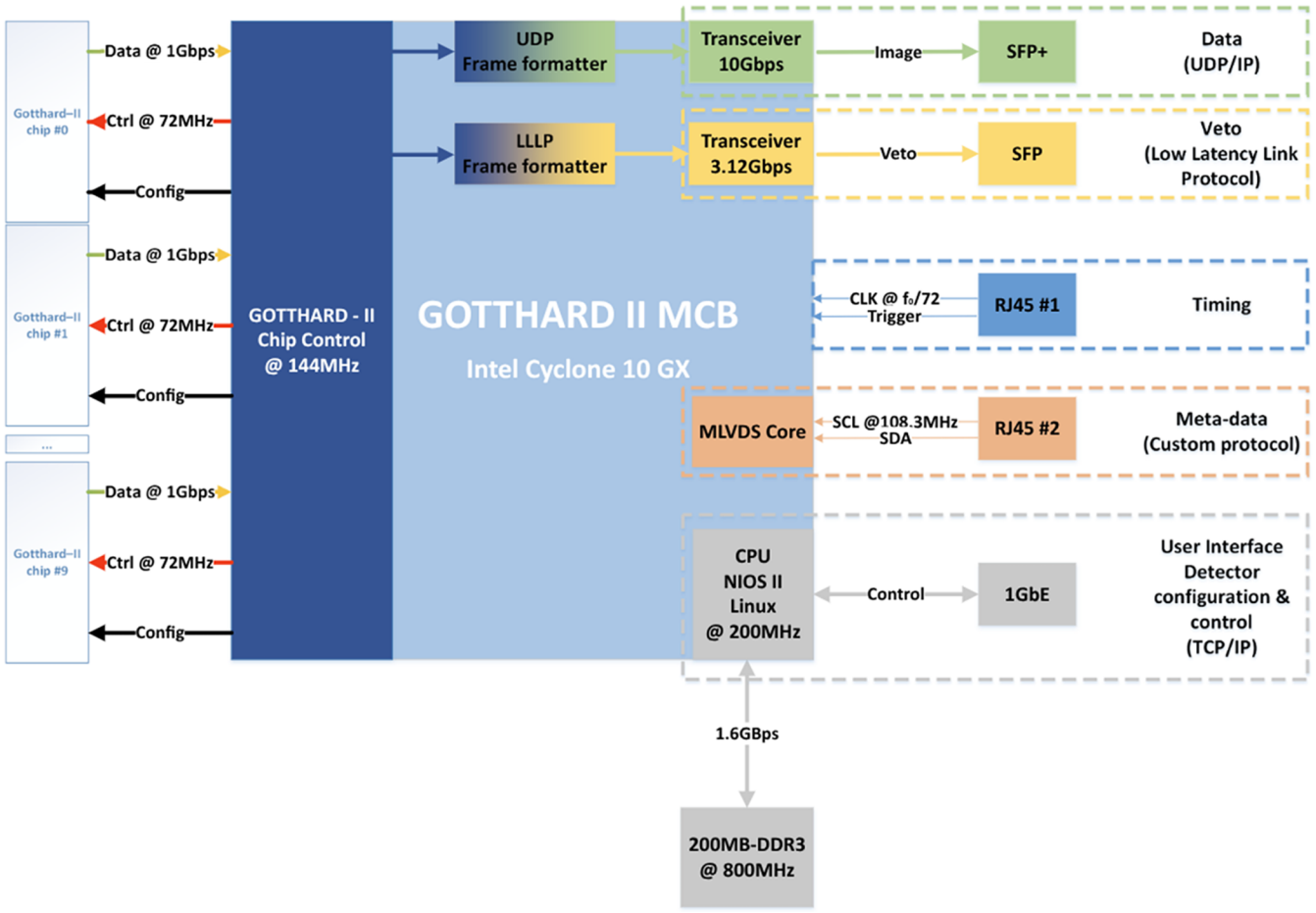

Figure 6. Firmware control diagram for the Intel Cyclone 10 GX model used in the Gotthard-II readout board. MCB: Main Control Board.

Additionally, one connector that provides access to the HV biasing line is reserved for calibration using sensor backside pulsing, as shown in Figure 4.

2.1.4. The Front-End Module. Figure 4 presents photographs of the design of the 50 and 25 μm pitch front-end modules (FEM). Each comprises a single silicon sensor, 10 or 20 ASICs, and 1 or 2 HDI connectors, respectively. Additionally, a capacitor array with up to 10 μF total capacitance is connected to the front-end module to filter noise from the sensor's high bias voltage generated by a DC/DC converter and to prevent voltage drops induced by photocurrent during high-flux X-ray incidence. Buffers for the ASIC bias voltages, generated by the digital-to-analog converters (DACs) on the readout board, are also implemented.

2.1.5. The Readout System and Interface. The readout system consists of a readout board and a timing board, as shown in Figure 5a. The readout board features an Intel Cyclone 10GX (CX)[13] Field-Programmable Gate Array (FPGA), 16 on-board DACs, two 10 Gbps SFP+ slots, a DC/DC converter for supplying high voltage to the sensor, a 128-pin connector, and other necessary components (*e.g.*, capacitors and resistors for signal decoupling and filtering).

The timing board includes two RJ45 connectors, a 3.125 Gbps SFP slot, an onboard quartz oscillator for clock generation, and a coaxial lemo connector. The timing board connects directly to the readout board via a 60-pin high-speed board-to-board connector.

Figure 5b shows the interfaces of the 50 μm pitch Gotthard-II detector. One of the two SFP+ slots on the bottom of the main board is used for detector control, interfacing with the client software, while the other slot is used to send image data from the detector to the receiver PC or server. The two RJ45 connectors at the top are dedicated to communicating with the EuXFEL timing system: one receives the clock and trigger, and the other receives serial data from the EuXFEL machine, such as the bunch train ID, bunch filling, and the decoding clock for the serial data. The SFP slot between the two RJ45 connectors is used to send out the veto information. For non-EuXFEL applications, the lemo connector receives the external trigger signal, and the onboard quartz generates the detector's clock. The BNC connector is used for detector calibration via sensor backside pulsing.

For the 25 μm pitch detector, an additional readout board is used, providing two extra SFP+ slots for detector control and data transmission, compared to the 50 μm pitch detector. The two readout boards receive the same clock, trigger, and metadata from one common timing board.

A detailed specification list for the Gotthard-II detector is presented in Table 1.

2.2. Detector Control and Communication. The Gotthard-II detector module is directly controlled by the FPGA on the readout board. The FPGA enables precise control of the detector's operation in all three operating modes through a dedicated serial interface, with a time resolution of the controlling signals below 7 ns, given by the internal clock

https://doi.org/10.1021/photonsci.5c00027
Photon Sci. XXXX, XXX, XXX−XXX

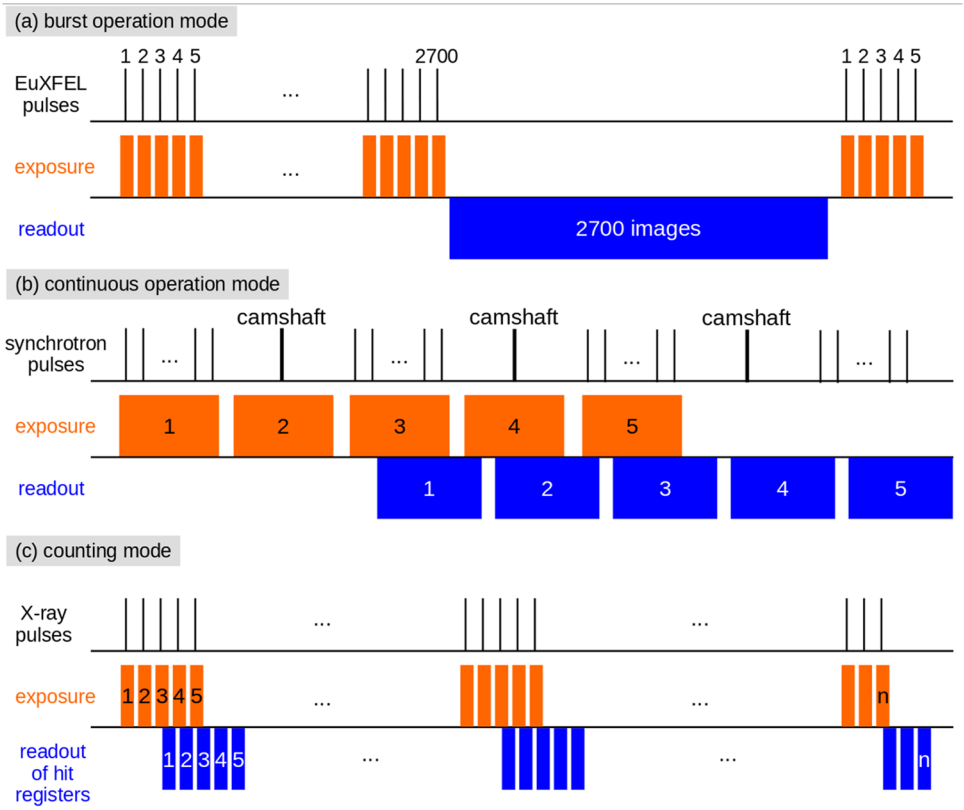

Figure 7. Three operation modes of Gotthard-II: (a) burst operation mode at a maximal frame rate of 4.5 MHz with a memory depth of 2700 images per burst, (b) continuous operation mode with a frame rate up to 400 kHz and a minimal exposure time of 55 ns for measuring Camshaft pulses, which are single isolated bunches with larger separation in time (~100 ns) from their neighboring bunches at synchrotrons, (3) counting mode at maximal 4.5 MHz frame rate with a 1-bit counter.

frequency of 144 MHz. In addition, the threshold for the comparator of each strip can be set when operating in counting mode or streaming veto signals for pixel detectors.

The other active elements on the readout board, such as the DACs for generating required bias voltages for the ASIC, the high-voltage DC/DC converter for sensor biasing, and the individual SFP+ sockets for data streaming and communication with the detector from the user, are also controlled by the FPGA. The separated sockets allow the connection of data streaming to a high-performance data network, while the less demanding detector communication can be connected to the facility's control network.

For high-performance data streaming, a UDP/IP protocol over a 10 GbE link is employed. Each Gotthard-II's 1D image is encapsulated in a single frame with a fixed size, containing 2560 Bytes of image data and 112 Bytes of metadata. The metadata includes essential information for a data backend application to interpret the image, such as the time the frame was captured, the acquisition settings, the detector ID, and, for the EuXFEL facility, the train ID and the bunch number within the train.

The other SFP socket is a 1 GbE link and is connected to a Nios II soft-core processor[14] instantiated in the FPGA, which runs a detector server in a Linux environment. Through the detector server, users have access to all settings and diagnostic information.

Additionally, the timing board attached to the readout board provides the Gotthard-II detector with clock and synchronization signals from the facility. Specifically for the EuXFEL, two interfaces are available alongside the clock and synchronization signals. The first interface allows the detector to receive metadata distributed by the EuXFEL machine. The 108 Mbps serial stream is decoded by the FPGA to extract information such as the train ID, which is later used to tag acquired data. The second interface is used to stream out veto information for each bunch to other detectors. This information is transmitted over a 3.125 Gbps link, following the EuXFEL Low Latency Link (LLL) protocol specification. The signal diagram of the FPGA is shown in Figure 6.

2.3. Detector Operation. The Gotthard-II detector operates in three modes, as shown in Figure 7: burst, continuous, and counting.

In burst mode, the detector captures images at a frame rate of up to 4.5 MHz using the internal ADCs and can store up to 2720 frames in its on-chip SRAM memory (20 more images than the number of EuXFEL pulses). The default exposure time is 110 ns at the highest frame rate. After all frames are stored in the on-chip SRAM, they must be read out before the next burst begins. The readout time for each frame is approximately 2.1 μs using the default 108 MHz readout clock, corresponding to a total of 5.7 ms for 2720 frames, which is much shorter than the spacing of 99.4 ms between bunch trains.

In continuous mode, the Gotthard-II detector captures frames at a rate of up to 400 kHz, with a minimum period of 2.5 μs. Since the Gotthard-II ASIC uses a pipeline architecture, the frames can be read out with a latency of 2.25 times the period. In continuous mode, the on-chip SRAM is bypassed, and the data is streamed out directly from the ASIC. The

https://doi.org/10.1021/photonsci.5c00027
Photon Sci. XXXX, XXX, XXX−XXX

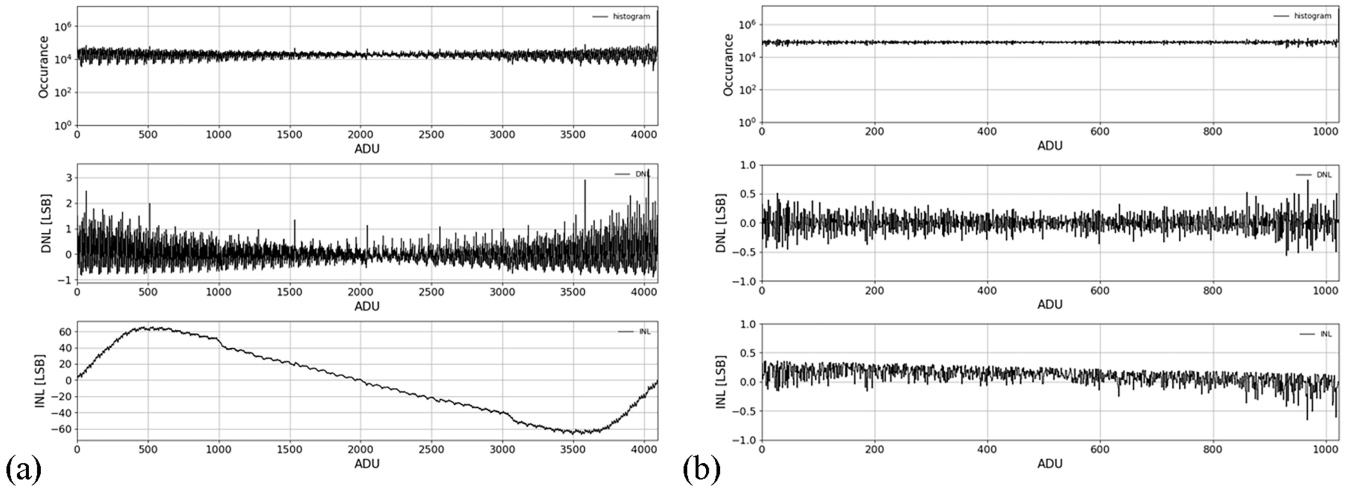

Figure 8. ADC performance and calibration. (a) 12-bit ADC raw output in a histogram test using a linear input covering the entire input range of the ADC and derived DNL and INL. (b) Histogram output, DNL, and INL at 10-bit after calibration.

default exposure time is 55 ns, which can be used to measure single isolated Camshaft bunches at synchrotrons.

In counting mode, the detector takes frames at a maximum rate of 4.5 MHz without writing them into the SRAM. Instead, the output of each channel after the ADC is compared to a 14-bit digital value of a threshold that can be set for each channel independently. If the output is above the threshold, a photon hit is registered and counted. The hit registers of all channels are then read out within 165 ns with a latency of 2.25 times the period of 220 ns. With further firmware implementations, the counts can be streamed out for each frame or summed over a certain number of frames by the FPGA for each strip channel and then sent out from the detector.

3. EXPERIMENTAL METHOD FOR DETECTOR CALIBRATION

For the charge-integrating Gotthard-II detector, the raw output from the on-chip ADC is in analog-to-digital units (ADU), which must be converted into either the measured energy or the number of photons at a given energy. This conversion requires several calibration parameters for the detector, including the offsets and conversion gains for each of the three gain settings for each strip channel. These parameters are generated separately for frames with "even" (frame-0,2,4,...) and "odd" (frame-1,3,5,...) indices due to the two analog capacitors connected to the preamplifier's output, which operate interleaved across different frames.[11] Thus, a total of 12 parameters must be calibrated for each channel.

Additionally, the SAR-ADCs implemented in the Gotthard-II ASIC provide a 12-bit digital output. These SAR-ADCs use a split-capacitor DAC architecture to achieve sampling and conversion rates exceeding 18 MS/s. For the DAC design, a bridge capacitor is implemented, splitting the DAC bank into two DAC arrays: LSB-DAC (Least-Significant Bits) with 5 capacitors and MSB-DAC (Most-Significant Bits) array with 6 capacitors. During the comparisons, either a higher or lower reference voltage is successively connected to each capacitor in the MSB-DAC after each comparison, making the voltage at the input of the ADC comparator increased or decreased by half. When the reference voltage starts to connect to the largest capacitor in the LSB-DAC, due to the capacitance mismatch of the bridge capacitor and parasitic capacitance, the voltage cannot be changed by half. Thus, this design introduces segmented linear outputs across different input ranges. Therefore, the ADCs must first be calibrated to achieve 10-bit resolution before further calibrating offsets and conversion gains.[10]

In this section, we will focus on the calibration of the 50 μm pitch detector. The same calibration methods and procedures also apply to the 25 μm pitch version. Unless otherwise specified, the detector is cooled to 20 °C using a liquid coolant.

3.1. ADC Calibration. The calibration of the ADCs within the Gotthard-II ASIC is performed using a histogram test method. A high-resolution (18-bit) DAC evaluation board (AD5781) is used to generate static input signals to calibrate the ADC. The input voltage is connected to one reference voltage of the differential buffer at the ADC input,[11] and it is scanned linearly with small voltage steps across the entire ADC output range. Based on the 12-bit ADC output, a histogram is generated with one bin per ADC value (0 to $2^{12}-1$), and the Differential Nonlinearity (DNL, a measure of the deviation from an ideal output set size for a given input range) and Integral Nonlinearity (INL, a measure of the maximum deviation from the ideal slope of the ADC measured from the center of the step) are calculated. The 12-bit ADC output is then corrected using the INL for each code, and the final 10-bit calibrated ADC value is obtained by reducing 2 bits from the 12-bit INL-corrected output.

These procedures generate a Look-Up Table (LUT) that allows the 12-bit ADC output to be converted to 10-bit. After this conversion, the DNL and INL are recalculated at the 10-bit resolution. Figure 8 illustrates the occurrence of a histogram test, along with the derived DNL and INL for both the 12-bit raw output (a) and the 10-bit calibrated output (b). The ADC calibration procedures are detailed in Zhang et al. 2021.[11]

3.2. Single Photon Detection and Conversion Gain. The conversion gain in ADC units per keV (ADU/keV) in G0 is calibrated using single monochromatic X-ray photons. The initial measurement was conducted with 12.6 keV X-ray photons at the Materials Science (MS) beamline of the Swiss Light Source (SLS). The Gotthard-II detector was positioned approximately 1 m from the beam exit and 10 cm below the direct beam. The monoenergetic X-ray beam was scattered in

https://doi.org/10.1021/photonsci.5c00027
Photon Sci. XXXX, XXX, XXX−XXX

the air and then measured by the Gotthard-II, as illustrated in Figure 9.

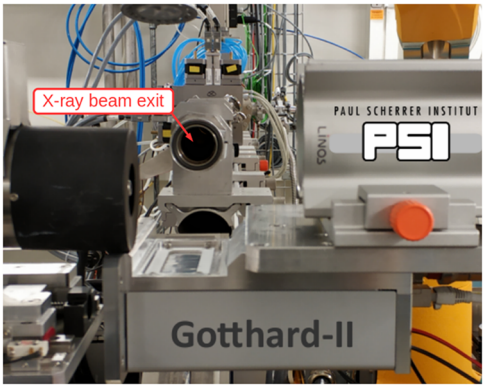

Figure 9. Measurement set-up for measuring air-scattered 12.6 keV X-ray photons at the Material Science (MS) beamline of the Swiss Light Source (SLS).

During the measurement, the detector was configured in burst mode with an exposure time of 1 μs, and 135 million frames were captured. Figure 10a and c display histograms of the outputs from a strip channel, both at 12-bit and 10-bit resolution before and after applying the LUT correction. Without applying additional corrections, the spectrum at 10-bit fluctuates significantly due to the imperfect DNL at 10-bit, as shown in Figure 10b. This fluctuation can be corrected using the DNL information for each code: $N_{10bit,corr}[i] = N_{10bit}[i]/(DNL_{10bit}[i]+1)$, where $DNL_{10bit}[i]$ is the DNL value for the same code. The corrected spectrum is shown in Figure 10d. The peak around 193 ADU corresponds to frames without a photon hit (noise peak), while the peak around 209 ADU represents frames with photon hits. The two peaks, corresponding to zero and one photon of 12.6 keV, were then fitted independently using a Gaussian function, as shown in Figure 10e, from which the centers of the two peaks were extracted. Figure 10f displays the extracted peak positions superimposed with a linear function. The conversion gain (ADU/keV) was determined from the slope of the linear function.

Since access to the beamline is not always possible, we also calibrated the detector using X-ray photons generated by a fluorescence target in combination with a commercial X-ray tube in the laboratory, such as the K_α-fluorescence of 17.5 keV from a molybdenum target and other metal targets. Due to the noise of the detector, K_α and K_β fluorescence photons cannot be separated in the histogram; owing to the much lower probability of K_β fluorescence compared to K_α, thus, the energy of the K_α-fluorescence is used to calibrate the conversion gain. In this setup, the experimental configuration is similar to that used at the MS beamline, except that the fluorescence target is tilted by 45° relative to the beam and positioned above the detector in the same configuration. The setup for measuring X-ray fluorescence photons has been documented elsewhere[15,16] and will not be discussed in detail here.

3.3. Noise. The noise of the Gotthard-II detector is determined from dark measurements. The detector was configured in burst mode with internal timing for 4.5 MHz operation. In this configuration, the default exposure time is 110 ns. The 10-bit output of each channel was plotted into a histogram and fitted with a Gaussian function, and the standard deviation was extracted from the fit. Values for all strip channels and their statistical distribution are shown in Figure 11a and b. The average standard deviation is 1.30 ± 0.11 ADU. From this value, the noise in electrons (e^-) r.m.s. was then calculated using the conversion gain determined from the single photon measurement. The noise and its statistical distribution are presented in Figure 11c and d. The nominal noise from the measurement is 278 ± 20 e^-.

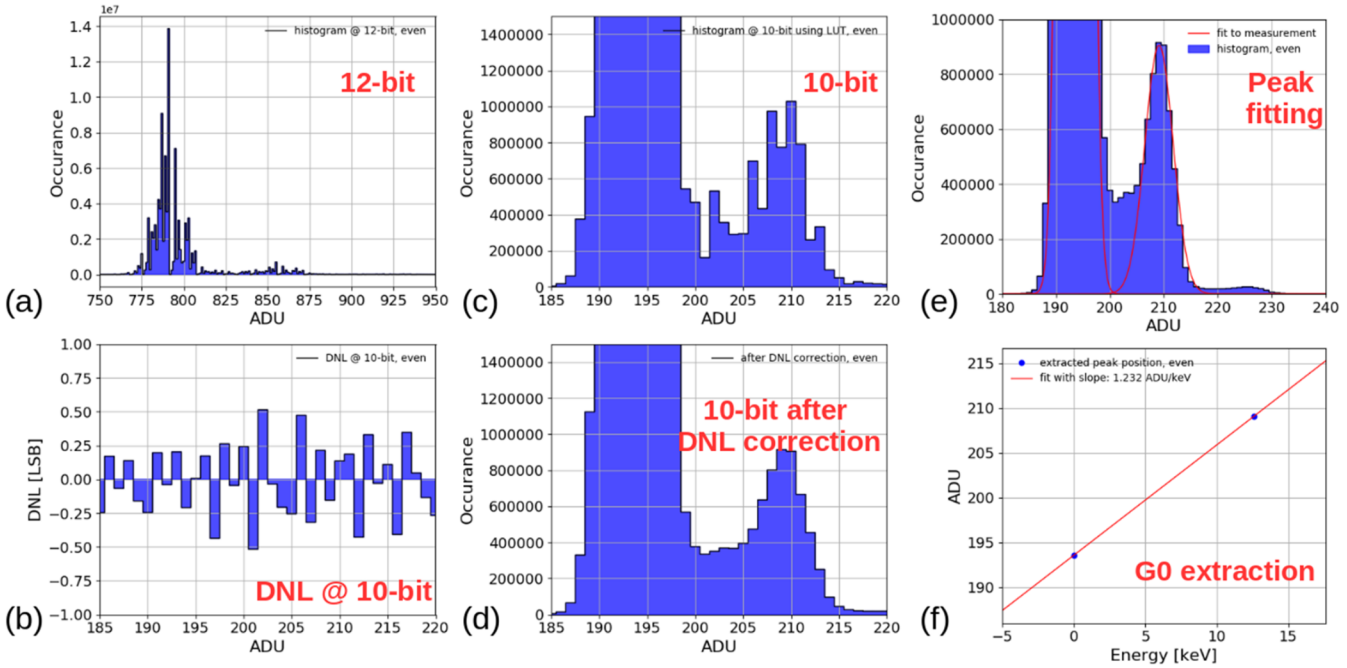

Figure 10. Single-photon detection of 12.6 keV X-rays using Gotthard-II: (a) and (c) Histograms at 12-bit and 10-bit output. (b) DNL at 10-bit. (d) DNL corrected histogram at 10-bit. (e) Gaussian fitting to the 0 and 1 photon peaks. (f) Linear function for the extraction of conversion gain.

https://doi.org/10.1021/photonsci.5c00027
Photon Sci. XXXX, XXX, XXX−XXX

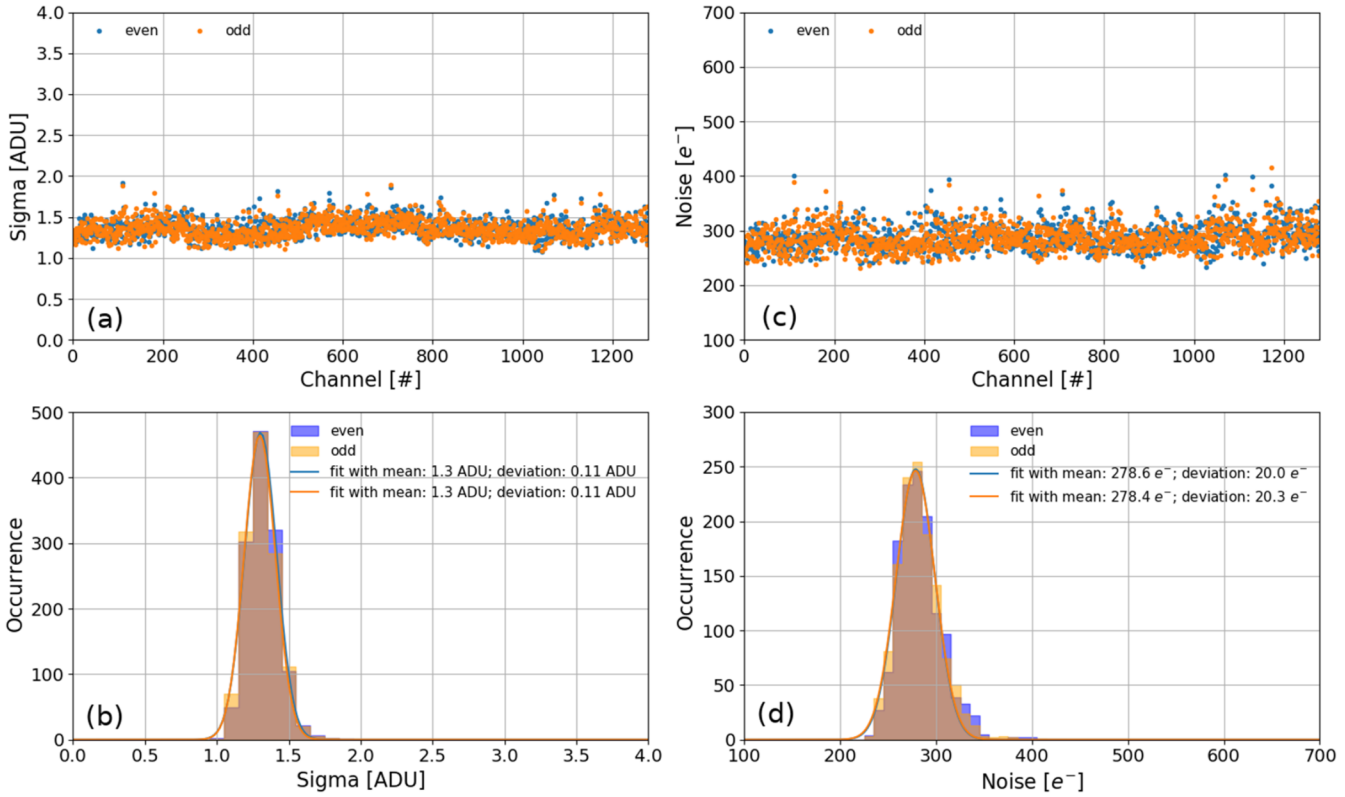

Figure 11. Noise in ADU and e⁻ r.m.s. for all strip channels and their distributions. (a) Noise in ADU for all strip channels, and (b) its distribution showing a mean value of 1.3 ± 0.1 ADU. (c) Noise in e⁻ r.m.s. for all strip channels, and (d) its distribution showing a mean value of 278 ± 20 e^-.

It is worth noticing that the noise strongly depends on the configuration of the Gotthard-II detector. Increasing the gain of the Correlated Double Sampling (CDS) from the default factor of 2.2 to 3.0 improves the noise by approximately 30%. Additionally, relaxing the tight timing requirements for EuXFEL operation allows for better noise filtering via the resistor before charging the analog capacitors,[11] as well as improved signal settling during the ADC sampling/comparison phase, leading to improved noise performance. Noise performance optimized for various experiments under different settings will be discussed in a separate manuscript.

3.4. Dynamic Range. For dynamic gain switching detectors such as AGIPD, Jungfrau, and Gotthard-I/II, one of the challenges is calibrating the conversion gains and offsets across three different gain settings: G0 (high gain), G1 (medium gain), and G2 (low gain). The calibration of offsets is particularly critical when operating the detectors in dynamic gain switching mode, as these offsets must be subtracted before applying the gain correction. Inaccurate calibration of the offsets in G1 and G2 can lead to discontinuities in the calibrated output when transitioning between different gain settings.[17,18] This occurs because the offsets are often calibrated with fixed gain settings in G1 or G2, in which case the extracted offsets are slightly higher or lower than the corresponding offsets in dynamic gain switching mode. Although the offset shift in ADU is small, the uncertainty becomes significant after applying the conversion gain, which is smaller in G1 and G2.

Therefore, it is crucial to calibrate both conversion gains and offsets in the same mode that will be used during experiments. This requires a calibration source capable of scanning the entire dynamic range.

In our study, we employ the backside pulsing technique to scan over the entire dynamic range.[19,20] Throughout the measurement, the silicon sensor of the detector is biased at 90 V above the full depletion voltage. A step signal generated by a wave generator is fed to an amplifier with a gain of 5, and the output of the amplifier is AC-coupled to the sensor's bias voltage. The step signal across a capacitor will generate a charge that can be measured by the detector. The rising edge of the input step signal ΔV_{inj} is aligned within the detector's exposure window. The measured charge, Q_{meas}, is given by $Q_{meas} = C_{strip} \cdot \Delta V_{inj}$, where C_{strip} is the strip capacitance to the backplane, provided C_{strip} is much smaller than the equivalent capacitance of the preamplifier input, which is $C_{pre} \cdot A_{dc}$ (i.e., $C_{strip} \ll C_{pre} \cdot A_{dc}$). A_{dc} is the DC gain of the pre-amplifier. For Gotthard-II, C_{strip} is 93.7 fF and 49.4 fF for 50 and 25 μm pitch strips, respectively, as calculated based on the strip's pitch and sensor thickness, the minimal C_{pre} in dynamic gain switching mode is approximately 40 fF (including parasitic capacitance), and A_{dc} is >1000,[10] satisfying the requirement of $C_{strip} \ll C_{pre} \cdot A_{dc}$.

The maximal injected voltage ΔV_{inj}^{max} to the microstrip sensor is 35 V, which generates a maximal charge of 3.3 and 1.7 pC in each channel of 50 and 25 μm pitch sensors. This corresponds to the charge produced by photons with a total energy of $7.4 \cdot 10^4$ and $3.9 \cdot 10^4$ keV, covering the entire range of G0 and G1 as well as most of G2.

Figure 12 shows the output of all strip channels of the Gotthard-II detector with different charge injections through backside pulsing. In the measurement, the injection was performed in 100 steps covering the input voltage range from 0.005 to 35 V, with a logarithmic increase in step size. The upper and lower rows of the plots display results from the

https://doi.org/10.1021/photonsci.5c00027
Photon Sci. XXXX, XXX, XXX−XXX

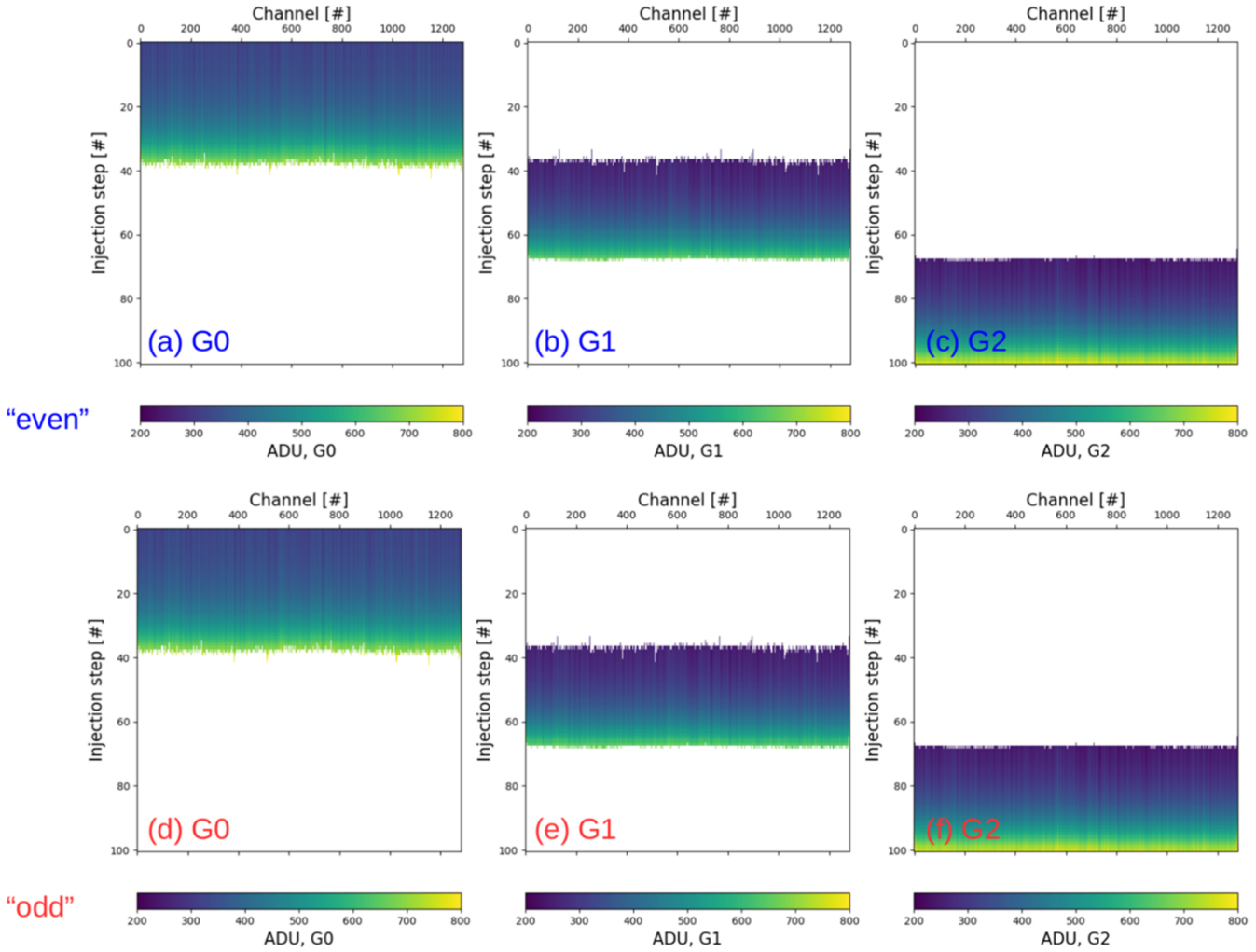

Figure 12. Dynamic range scan using sensor backside pulsing in G0, G1, and G2 for "even" and "odd" frames. The output has been converted to a 10-bit ADC value after applying the 12-bit to 10-bit LUT. (a)−(c) Output of all strip channels in G0, G1, and G2 for "even" frames as a function of the voltage injection step. (d)−(f) Output of all strip channels in G0, G1, and G2 for "odd" frames as a function of the voltage injection step.

"even" and "odd" frames. The output was converted to a 10-bit ADC value using the 12-bit to 10-bit LUT obtained from the ADC calibration. Additionally, according to the gain bit values, the output in the three gain regions—G0, G1, and G2—was plotted separately.

From these measurements, the outputs of each strip channel in G0, G1, and G2 were fitted with a linear function, and the slopes and offsets were extracted. Figure 13 shows the linear fit to the output at 10-bit from the dynamic range scan, along with the residual between the fit and the data for "even" frames (a & b) and "odd" frames (c & d) of a single strip (strip-15) as an example. The uncertainty of the residual, particularly in the high gain G0, is mainly due to fluctuations in the injected charge from backside pulsing, convoluted with the electronic noise in the readout ASIC.

Using the slopes extracted from the linear fit in each gain, the slope ratios between G0 and G1, and G0 and G2 were obtained. With the conversion gain in G0 measured using single X-ray photons, the conversion gains in G1 and G2 were determined. Figure 14 shows the calculated conversion gains and offsets in G0, G1, and G2. Figure 15 presents the statistics of the conversion gains and offsets, showing a gain dispersion (r.m.s.) of less than 7.5% and an offset dispersion of less than 10%.

The dynamic range of each strip channel was determined by taking the maximum possible output at 10-bit (i.e., 1023), subtracting the offset in G2, and then dividing by the conversion gain of G2. The dynamic range, expressed as the number of 12.4 keV X-ray photons, for all strip channels and their statistics are shown in Figure 16. The nominal dynamic range is 8700−8800 12.4 keV photons (total energy > 10^5 keV within specifications), with a 10% dispersion according to the histogram statistics. The nonlinearity of the detector output is less than 1% over the entire dynamic range, as reported in Zhang et al., 2021.[11]

The nominal offset in G2 at the 10-bit output is approximately 220 ADU. Lowering the offset in G2 by reducing the reference voltage can increase the dynamic range by an additional 20%. It should also be noted that if a higher CDS gain is selected, the noise performance can be improved, but at the cost of reducing the dynamic range by (3.0−2.2)/2.2 = 36%.

3.5. Temperature Dependence of Calibration Constants. To verify the influence of temperature on the calibration constants, a dynamic range scan was performed over a temperature range from 10 °C to 25 °C in 5 °C steps, representing commonly used operating temperatures. Figure 17a and b show the 10-bit output of the detector as a function

https://doi.org/10.1021/photonsci.5c00027
Photon Sci. XXXX, XXX, XXX−XXX

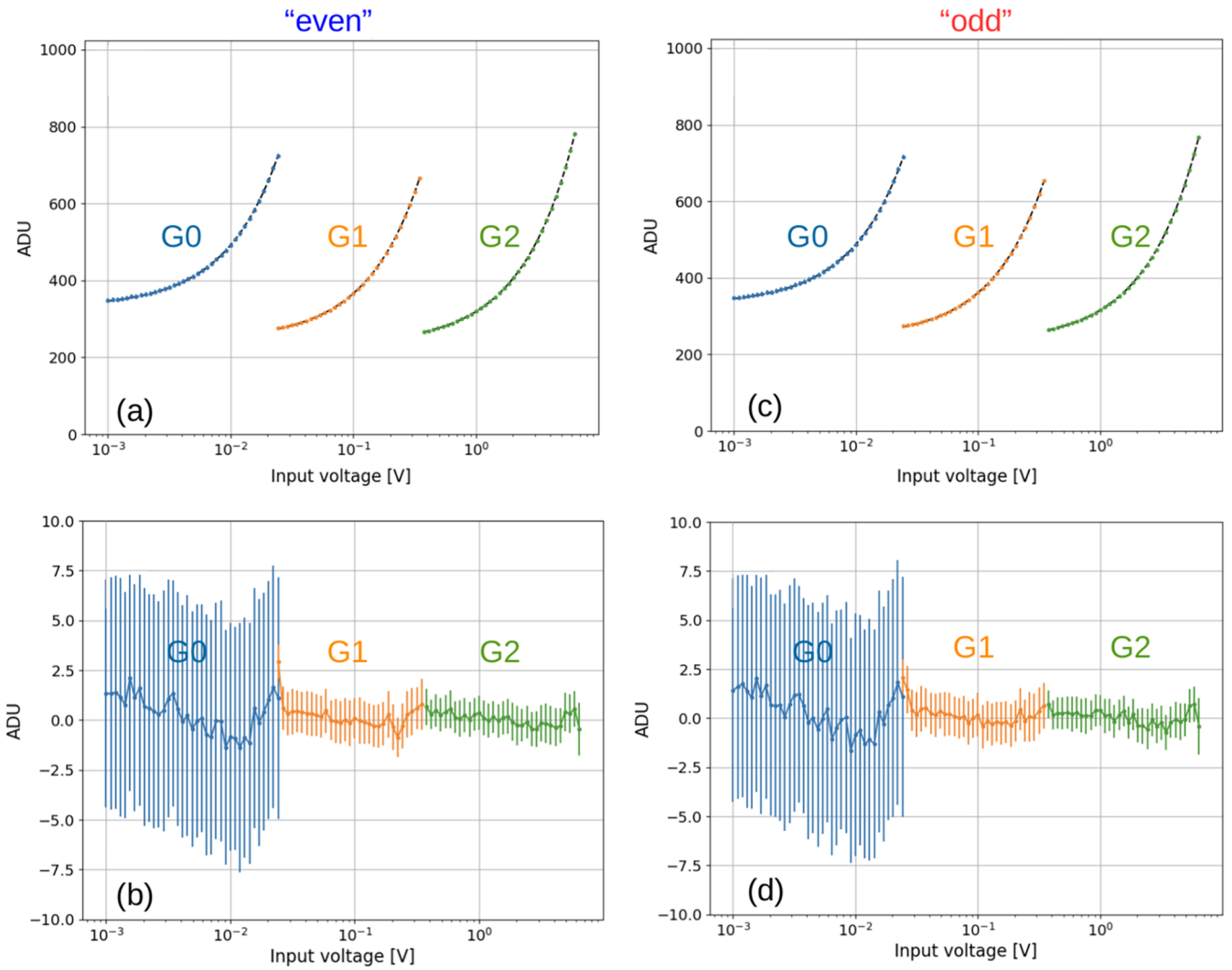

Figure 13. Dynamic range of a single strip channel (strip-15), as an example, shows in (a) and (c) the linear fit of G0, G1, and G2 and the residual of the linear fit in (b) and (d) from "even" frame indexes and "odd" frame indexes.

of injected voltage through backside pulsing and the number of photons, expressed in 12.4 keV X-ray photons, after calibration. The dynamic range curves overlap well in G1 and G2 across this temperature range. However, in G0, the outputs show a slight difference in ADU values due to the increased leakage current in the sensor with rising temperatures. At room temperature, the leakage current changes by approximately 8% for each 1°C variation.[21]

From the dynamic range scan, the conversion gains and offsets were extracted for different temperatures. Figure 18 presents the statistics of the difference in conversion gain (a–c) and offset (d–f) for each temperature, with 10 °C as the reference. The results indicate a minor change in conversion gain by less than 0.5% (nominal value) in G0, G1, and G2. The temperature dependence of the offsets is more significant in G0, with a maximal difference of up to ∼20 ADU between 25°C and 10 °C, corresponding to approximately 15 keV in energy. However, the offset difference is negligible in G1 and G2 due to the reduction in conversion gain after gain switching.

These measurements suggest that within a small range of operating temperature variations, the calibrated conversion gain remains valid for experiments. However, it is recommended to perform dark measurements and correct the appropriate pedestal values at the corresponding temperature.

4. RESULTS FROM EXPERIMENTAL VALIDATION

The Gotthard-II detector has been tested during several pilot experiments to validate its performance for future user experiments. The measurements conducted include (1) X-ray diffraction (XRD), (2) X-ray emission spectroscopy (XES), and (3) continuous measurements at the maximum frame rate of 400 kHz.

4.1. X-ray Powder Diffraction. The XRD experiment was conducted at the MS beamline of the SLS, which was equipped with a spectrometer based on Mythen-II[22] (Bergamaschi et al., 2010). Mythen-II detectors, before their upgrade to Mythen-III,[23−25] are well-established photon-counting microstrip detectors using 320 μm thick silicon sensors for XRD experiments at the MS beamline. The detector has now been upgraded to Mythen-III.[26] In the experiment, a silicon powder was filled into a capillary and used as the diffraction sample for this measurement. The experimental setup is shown in Figure 19a. The Gotthard-II detector was mounted on the spectrometer mechanics alongside 48 Mythen-II modules via an adapter plate. The sensor area of Gotthard-II was aligned

https://doi.org/10.1021/photonsci.5c00027
Photon Sci. XXXX, XXX, XXX−XXX

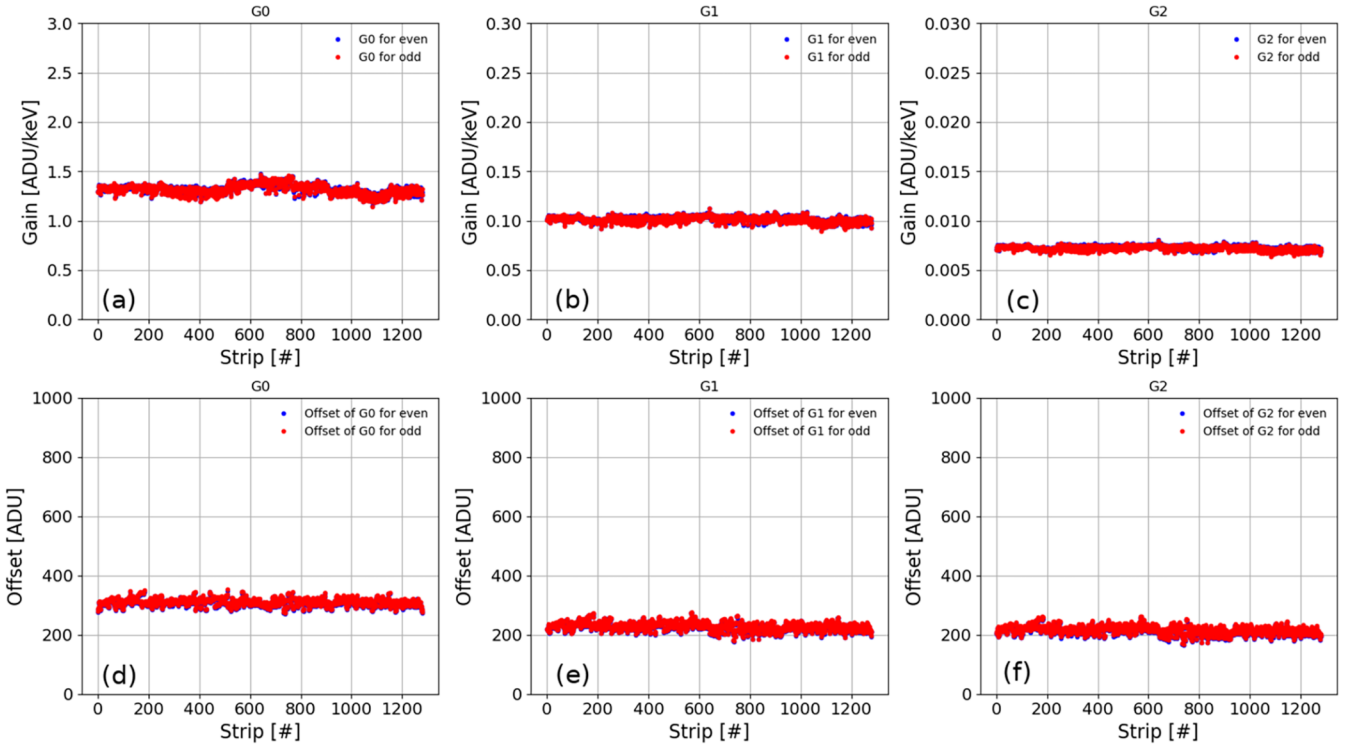

Figure 14. Gain and offset of all strip channels from one Gotthard-II 50 μm pitch module in different gains. (a)−(c) Gains of G0, G1 and G2. (d)−(f) Offsets of G0, G1, and G2.

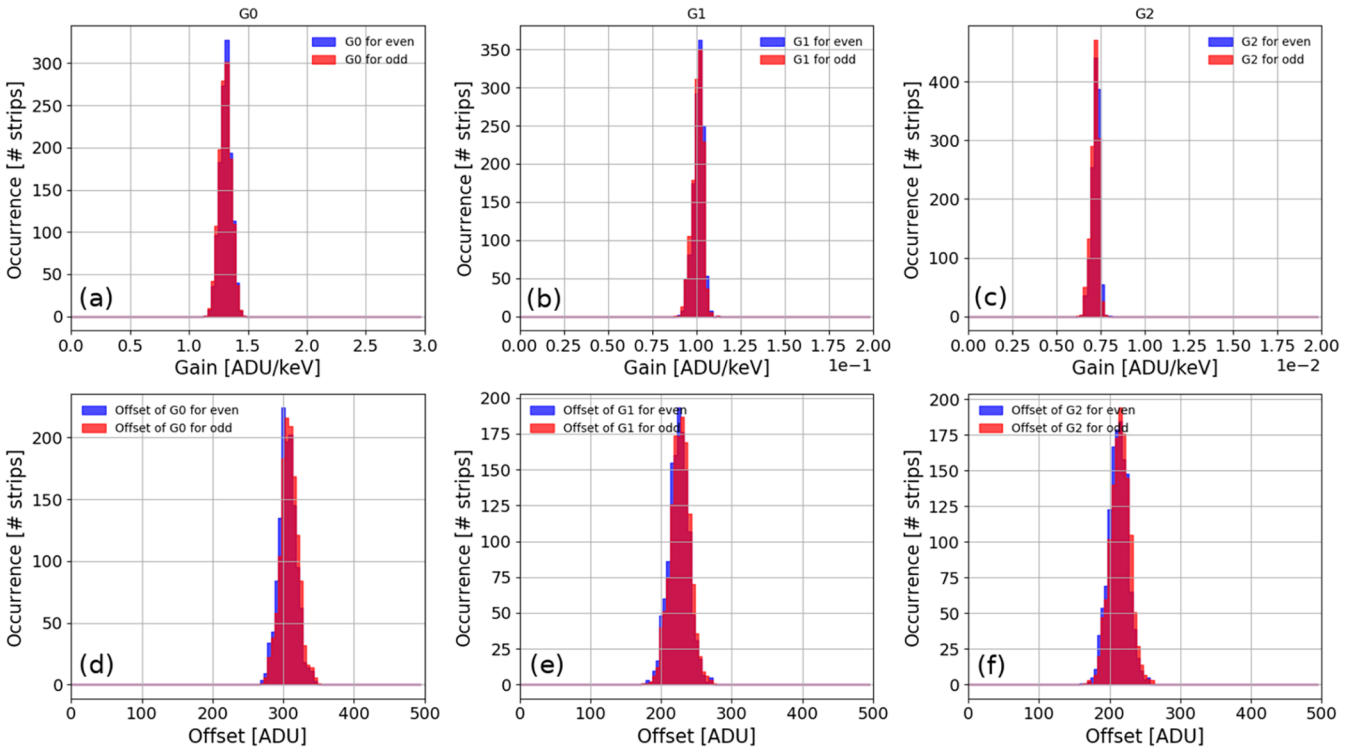

Figure 15. Histograms of gains and offsets in G0, G1, and G2 from one Gotthard-II 50 μm pitch module show a channel-to-channel dispersion of <7.5 and <10% respectively. (a)−(c) Histograms of gains. (d)−(f) Histograms of offsets.

with the Mythen-II sensing area and the plane of the X-ray photons. The distances from the sensor plane to the sample were 76 cm for Mythen-II and 89 cm for Gotthard-II. Mythen-II was used to acquire the diffraction data and served as a reference for comparing the results with Gotthard-II. Since the Mythen-II detectors covered a larger angle (120° in this case), the measurement was performed without moving the spectrometer for Mythen-II. For Gotthard-II, measurements were taken repeatedly at different angles, covering from 5° to −61° in 3° steps (23 steps in total). During the experiment,

https://doi.org/10.1021/photonsci.5c00027
Photon Sci. XXXX, XXX, XXX−XXX

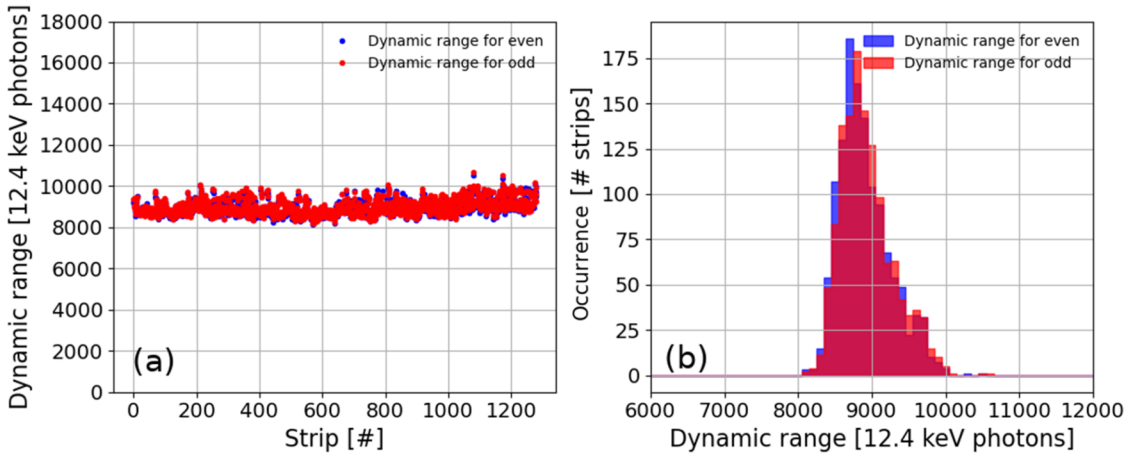

Figure 16. Dynamic range of the Gotthard-II detector with the default settings. (a) Dynamic range of all strip channels. (b) Histogram of dynamic ranges.

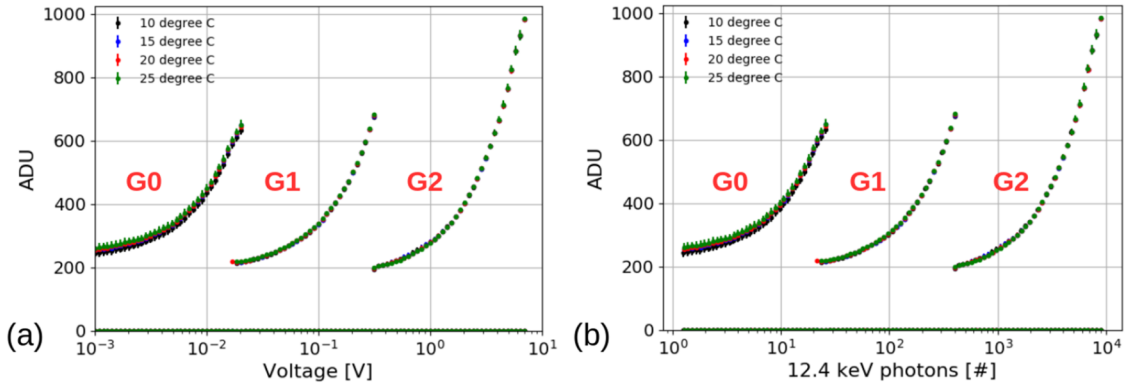

Figure 17. Dynamic range scan using backside pulsing was performed at different temperatures. (a) Detector 10-bit output vs. pulser input. (b) Detector 10-bit output vs. 12.4 keV X-ray photons.

12.6 keV X-ray photons were used. Due to the high intensity of the X-ray beam and the large interaction cross-section, the total data-taking time for Mythen-II was 1 s. Gotthard-II was configured in burst mode, with an exposure time of 1 μs, and 1 million frames were captured (1000 bursts containing 1000 images each) at each angle, corresponding to a total exposure time of 1 s. Thus, the results from both Mythen-II and Gotthard-II can be compared under similar running conditions.

Figure 19b presents the detector output expressed as the number of detected 12.6 keV X-ray photons versus the 2θ angle (Mythen-II in blue; Gotthard-II in red). The output has been normalized based on: (1) the angular coverage of the detection area of each strip due to the distances of the sensor planes of Mythen-II and Gotthard-II to the sample, and (2) the detection efficiency due to the different thicknesses of the silicon sensors used by the two detectors (70.2% for Mythen-II with a 320 μm thick sensor vs. 81.8% for Gotthard-II with a 450 μm thick sensor). The angular coverage contributes a scaling factor of 1.37, while the detection efficiency contributes 0.858, resulting in a total scaling factor of approximately 1.18.

4.2. X-ray Emission Spectroscopy. X-ray Emission Spectroscopy (XES) is a photon-in, photon-out technique widely used to determine the electronic structure of materials, such as local charge and spin density.[27−30] With the Gotthard-II detector, we have conducted XES measurements using standard test samples with known properties at both synchrotrons and Free-Electron Lasers (FELs). The results from Gotthard-II have been compared with those obtained using established detectors at these beamlines.

4.2.1. XES at Synchrotron. The first X-ray Emission Spectroscopy (XES) measurements with Gotthard-II were conducted at the SuperXAS beamline of the SLS. The experimental setup, depicted in Figure 20a, involved mounting an iron (Fe) foil on the sample holder at a 45° angle to the direct beam. This foil was irradiated by a monochromatic X-ray beam with a photon energy of >7.1 keV, slightly above the Fe K_β-edge (7.059 keV). The emitted fluorescence photons from the Fe foil were energy-dispersed in the vertical direction using a bending crystal, depending on the targeted fluorescence energy. For the Fe K_α fluorescence line, a bending crystal of germanium (Ge) with a ⟨220⟩ orientation was used. Figure 20c shows the sketched the side view and top view of the experimental configuration.

The Gotthard-II detector was positioned above the sample holder and aligned in the same plane as the sample. It was configured in continuous mode with an exposure time of 2.5 μs and triggered by an external trigger of 260 kHz (corresponding to a period of approximately 3.8 μs), synchronized to the synchrotron beam. This synchronization ensured that the number of bunches measured in all frames was consistent. In total, 1 million frames were captured, corresponding to a total exposure time of 2.5 seconds.

https://doi.org/10.1021/photonsci.5c00027
Photon Sci. XXXX, XXX, XXX−XXX

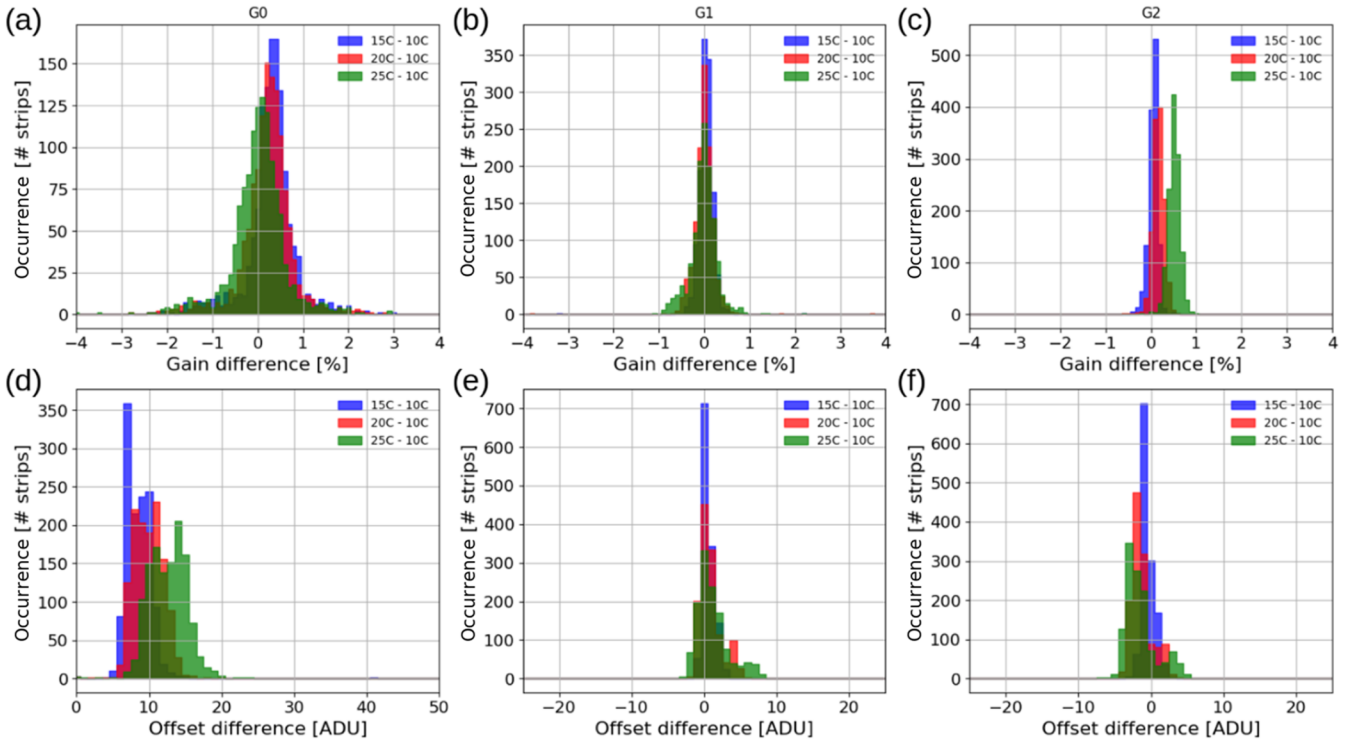

Figure 18. Temperature dependence of gain and offset in G0, G1, and G2. (a)−(c) are the statistics of the difference of the conversion gain at a given temperature with respect to 10 °C as a reference. (d)−(f) are statistics for the offsets at different temperatures.

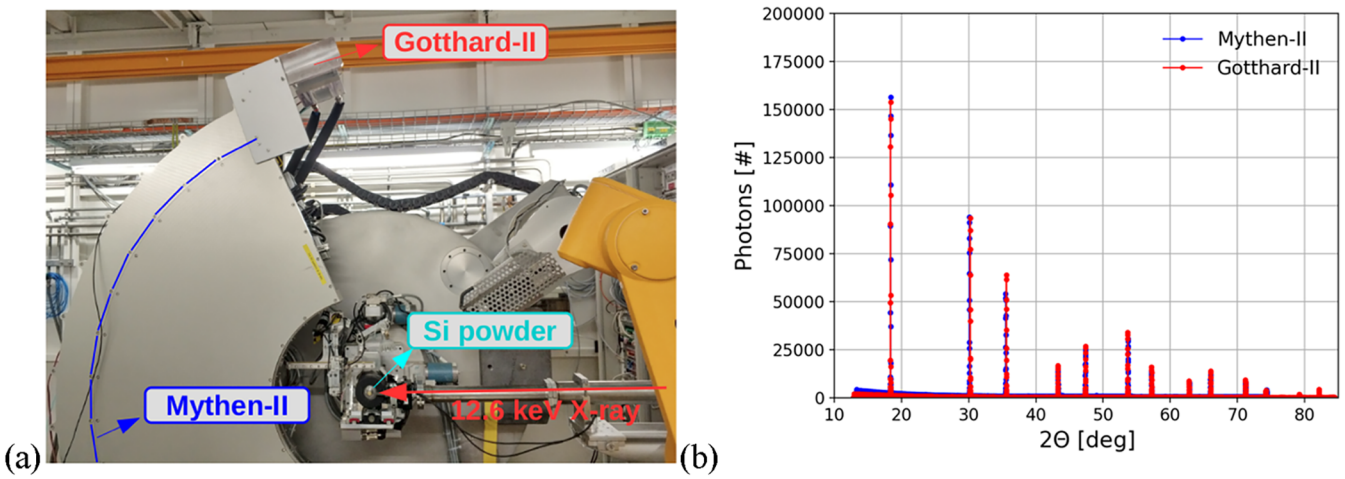

Figure 19. X-ray diffraction (XRD) measurements done at the MS beamline of the SLS: (a) experimental set-up with a single Gotthard-II module mounted on the same arc where the 48 Mythen-II modules are mounted, and (b) comparison of results between the Mythen-II and Gotthard-II detectors with the same counting/exposure time of 1 s.

For comparison, a Pilatus 100k detector—a photon-counting pixel detector with a pixel size of 172 μm—was also utilized in the same measurement configuration. The data-taking time for the Pilatus detector was 1 s. The 2D image from this detector, shown in the inset of Figure 20a, was projected along the vertical direction, and the pixel indexes were calibrated to the photon energy based on the two peak positions of $K_{\alpha 1}$ (6.404 keV) and $K_{\alpha 2}$ (6.391 keV). The same procedure to calibrate the strip channels to photon energy was applied to Gotthard-II as well. However, to compare the results under equivalent conditions, the outputs from Gotthard-II, converted to the equivalent number of 6.4 keV photons, were scaled down by a factor of 1/2.5 to normalize to the same 1 s exposure as the Pilatus, and further scaled by 3.44 to account for the difference in pixel/strip pitch. This resulted in an overall scaling factor of 1.376 for Gotthard-II's outputs.

Figure 20b compares the measured $K_{\alpha 1}$ and $K_{\alpha 2}$ spectra from the Pilatus 100k detector (in blue) with Gotthard-II (in red). The Pilatus detector shows overlapping $K_{\alpha 1}$ and $K_{\alpha 2}$ fluorescence photons with signals from scattered photons in the air, which can be attributed to the short distance from the sensor layer to the detector's entrance window. In contrast, the Gotthard-II detector shows the XES spectrum with significantly lower background photons. As shown in Figure 20c,d, the entrance window of Gotthard-II, positioned approximately 7 mm from the sensor plane, only allows fluorescence photons

https://doi.org/10.1021/photonsci.5c00027
Photon Sci. XXXX, XXX, XXX−XXX

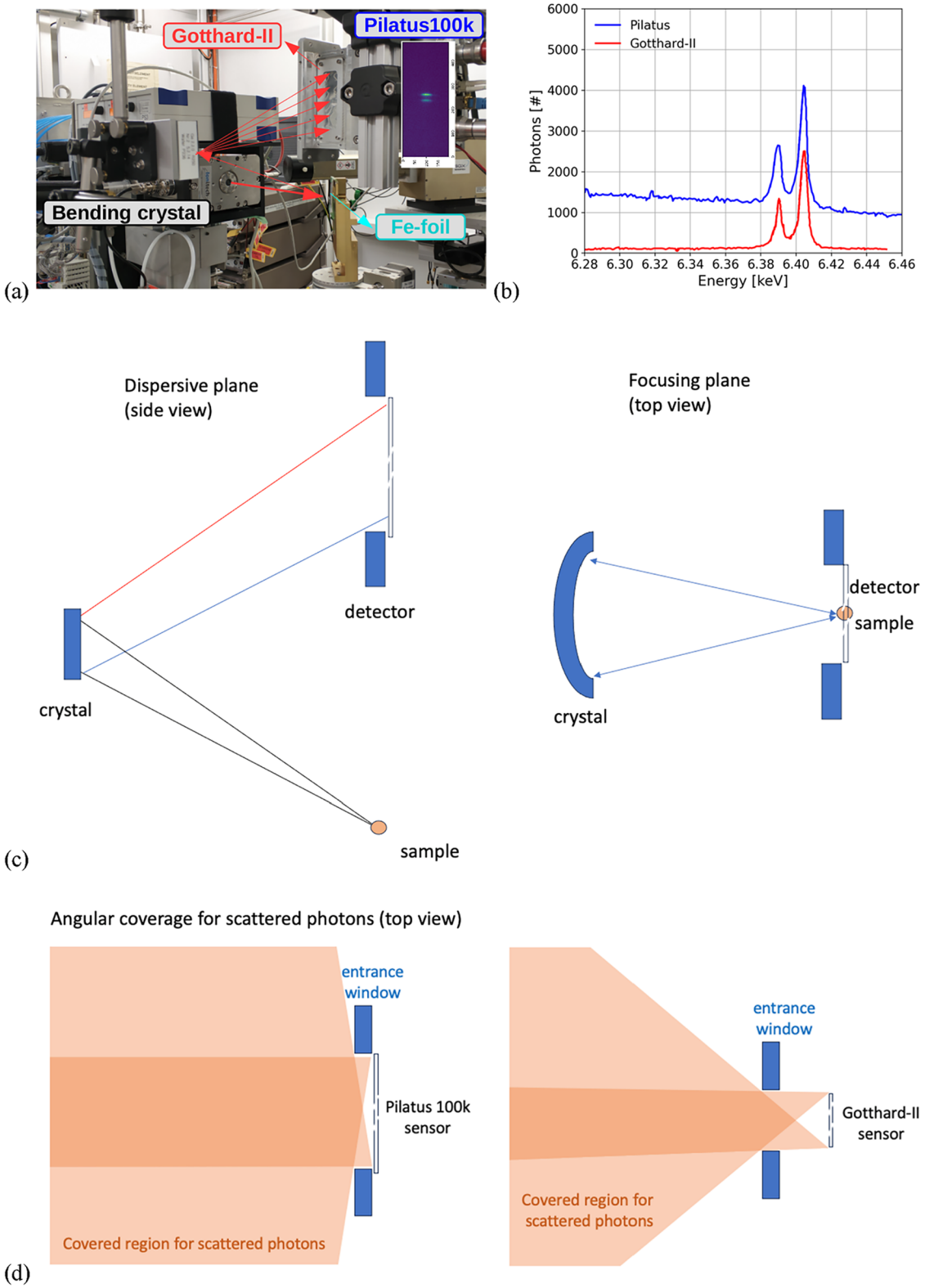

Figure 20. XES measurements at the SuperXAS beamline of the SLS: (a) Experimental setup. (b) Comparison of the XES spectra obtained with the Pilatus 100 k detector and Gotthard-II. (c) Side view and top view of the experimental configurations. (d) Sketch showing low background scattered photons measured with Gotthard-II compared to the Pilatus 100 k detector (not to scale).

within a certain solid angle to be measured, effectively blocking background signals from scattered photons coming from a broader angle.

In addition, the K_β fluorescence of the Fe foil (7.059 keV) was measured using the Gotthard-II with a bending crystal made out of silicon oriented at ⟨531⟩ to disperse the X-ray photons vertically. The same exposure time of 2.5 μs was set, and 100 million frames were recorded to detect the Valence-to-Core (VTC) signal[31] at a higher energy range (between 7.10 and 7.11 keV), despite a much smaller cross-section. Figure 21

https://doi.org/10.1021/photonsci.5c00027
Photon Sci. XXXX, XXX, XXX−XXX

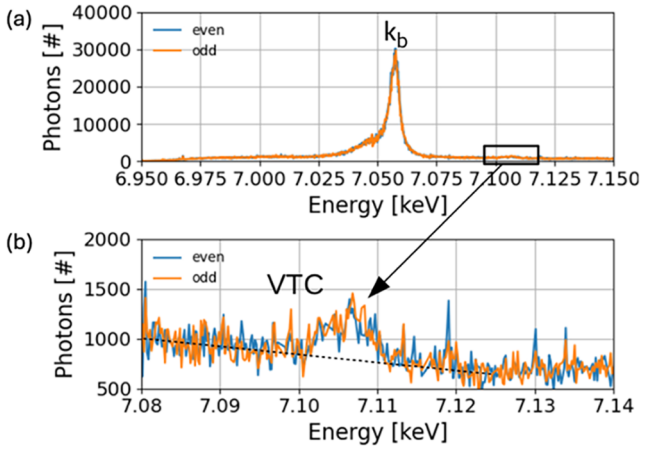

Figure 21. K_β fluorescence and VTC signal were measured with Gotthard-II at the SuperXAS beamline using a standard Fe foil target for testing purposes.

shows the XES spectra of the K_β fluorescence and VTC in a zoomed region. The VTC signal is distinctly visible, with a count of less than 500 photons per channel sitting on a background of 500 to 1000 photons, despite the total exposure time being only 250 seconds. This measurement demonstrates the capability of Gotthard-II in detecting signals from processes with low interaction cross-section. For user experiments, it is recommended to capture more images to increase the statistical reliability of such weak signals and potentially use the a high gain setting of CDS to improve the signal-to-noise ratio.

4.2.2. XES at the EuXFEL. A second XES experiment was conducted at the FXE beamline of the EuXFEL[32,33] using the Gotthard-II detector operated in burst mode with a frame rate exceeding 1 MHz, designed to measure each FEL pulse (proposal Nr 3225, DOI: 10.22003/XFEL.EU-DATA-003225-00). The FEL generated 140 bunches at a fundamental repetition rate of 560 kHz within a train (trains arriving at a 10 Hz frequency). The photon energy was set at 9.3 keV to excite a Cobalt(III) acetylacetonate complex ($Co(acac)_3$) in acetonitrile solution with a concentration of 30 mmol. The standard setup for liquid chemistry experiments,[34] depicted in Figure 22a, included the solution sample delivered in a 100 μm thick liquid jet with a flow rate of 30 mL/min. The Co $K\alpha_{1,2}$ fluorescence emitted by the solution was dispersed in the vertical direction using seven Si(531) cylindrically bent crystal analyzers (0.5 m radius) mounted on the von Hamos spectrometer at the FXE beamline. The Gotthard-II and a Jungfrau 1M detectors were mounted side-by-side on the robot arm to sequentially measure the XES spectra and compare them. Both detectors were aligned on the same plane at equal distances and solid angles relative to the von Hamos spectrometer. The experimental setup is shown in Figure 22a.

During the measurement, the Gotthard-II was configured to a 1.1 MHz frame rate in burst mode with an exposure time of 440 ns, capturing 2700 images per burst. The FEL pulses were tuned to a 1.1 MHz repetition rate as well. The correlated-double sampling (CDS) gain of the detector was set high to enhance noise reduction and increase sensitivity to single photons. The detector was triggered at 10 Hz, synchronized with the clock of each bunch train, with FEL pulses measured in every second frame by Gotthard-II. The XES spectra from all single FEL pulses were summed up. Conversely, the Jungfrau 1M detector was set to continuous mode with a frame rate of 10 Hz. An exposure of 600 μs was configured to measure all pulses in a train, with the 2D images projected along the vertical axis and spectra from all measured trains subsequently summed up.

The x-axes of the XES spectra from Jungfrau and Gotthard-II were calibrated to photon energy based on the energies of the $K_{\alpha1}$ (6.930 keV) and $K_{\alpha2}$ (6.915 keV) fluorescence lines of Cobalt. The outputs of the two detectors (y-axis) were then normalized to their respective spectral integrals for comparison. Figure 22b presents the comparative XES spectra of the Jungfrau and Gotthard-II detectors following energy calibration and spectral normalization. The results demonstrate a good agreement between the two detectors, despite being operated in different modes for this measurement. Beyond the summed spectra, Gotthard-II also offers the unique capability to detect each pulse in pump-probe experiments with high repetition rates.

Pump-probe experiments using the same sample have also been performed at a lower FEL repetition rate and reported in Ramilli et al., 2024.[35] With the commissioning of Gotthard-II at the spectrometer of the FXE beamline, more pump-probe

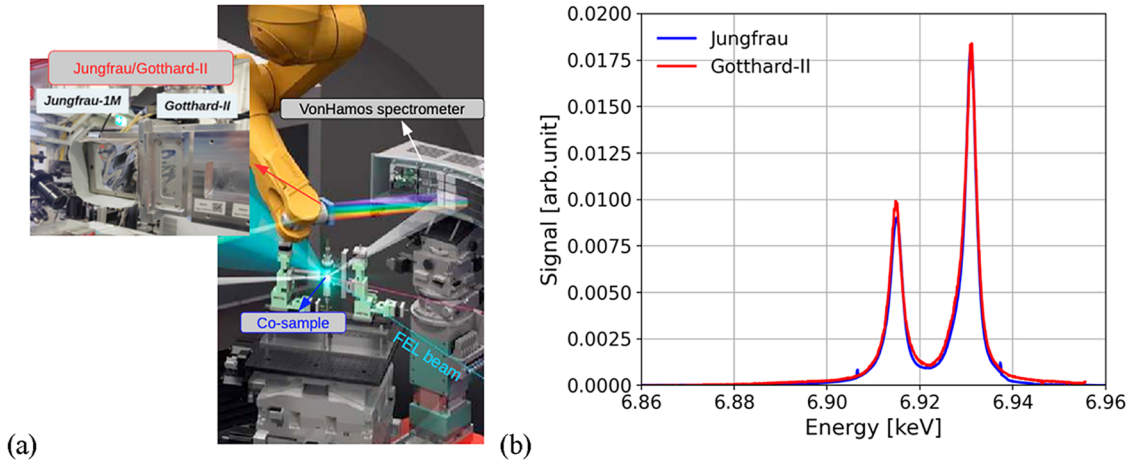

Figure 22. XES experimental tests at the FXE beamline of the EuXFEL: (a) measurement setup showing both Jungfrau and Gotthard-II detectors mounted on the same robot arm, (b) comparison of the XES spectra between the two detectors.

https://doi.org/10.1021/photonsci.5c00027
Photon Sci. XXXX, XXX, XXX−XXX

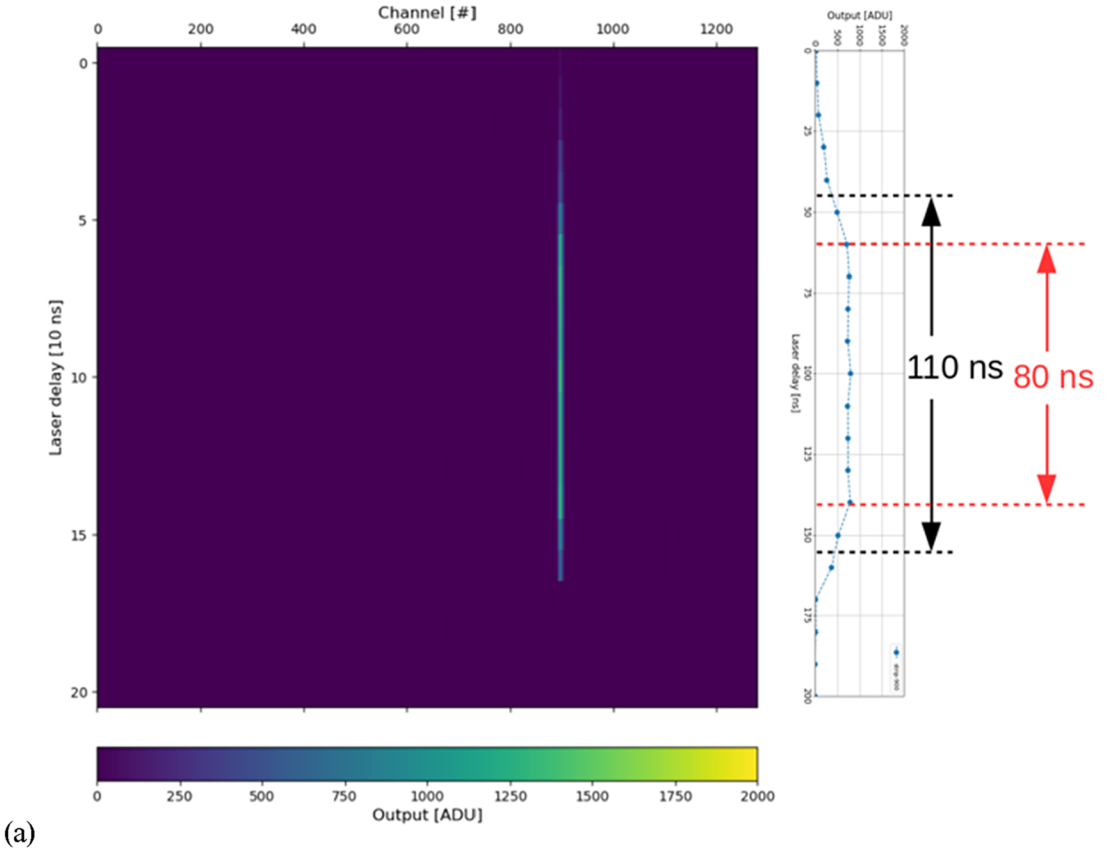

(a)

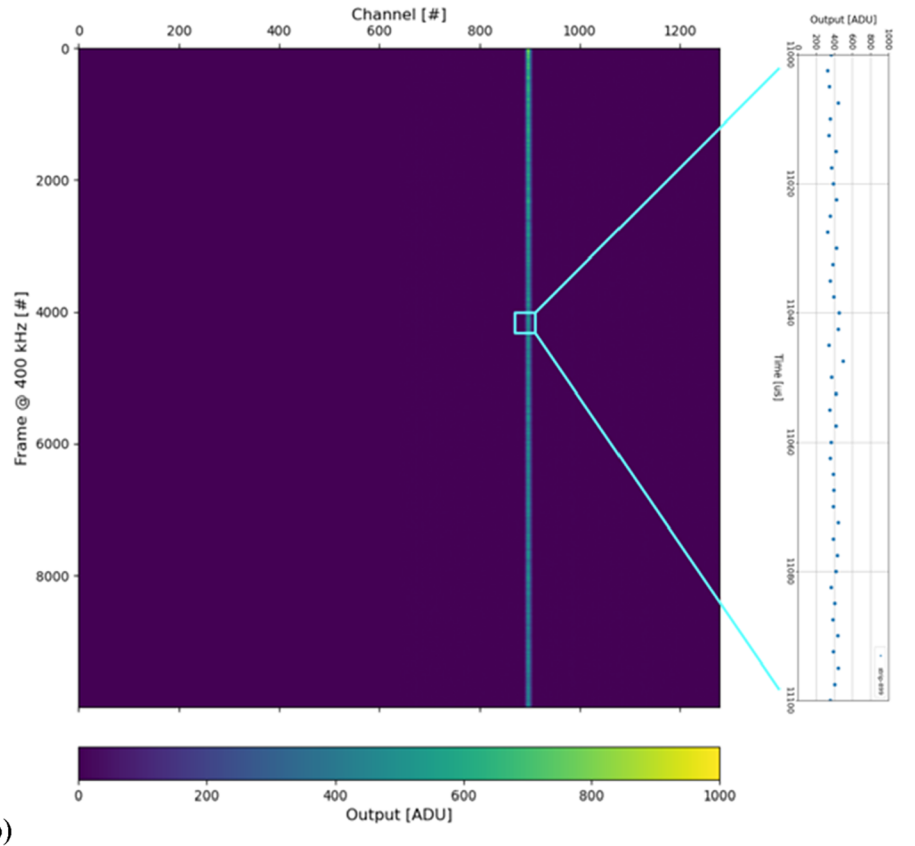

(b)

Figure 23. (a) The delay scans at 400 kHz frame rate using laser injection. (b) Continuous imaging at 400 kHz frame rate with Gotthard-II synchronized with the infrared laser at the same repetition rate.

https://doi.org/10.1021/photonsci.5c00027
Photon Sci. XXXX, XXX, XXX−XXX

experiments using single FEL pulses have been performed and will be reported in a separate paper.

4.3. Continuous Imaging at 400 kHz. To assess the capability of Gotthard-II for continuous imaging in synchrotron applications and future Free-Electron Lasers (FELs) operating in CW mode at high repetition rates, additional laboratory tests were conducted at the 400 kHz frame rate, currently limited by its readout system.

The Gotthard-II was set to continuous mode with an exposure time of 110 ns (minimum 55 ns), and it was triggered using an external signal at 400 kHz, corresponding to a period of 2.5 μs. This same trigger signal was also sent to a wave generator, which was configured to generate signals at 400 kHz but with a tunable delay relative to the original trigger. The signals from the wave generator then triggered a pulsed infrared laser (~500 ps) with a wavelength of 1030 nm. The laser was directed onto the silicon sensor of the Gotthard-II, inducing detectable signals within the detector.

Figure 23a shows the result of the laser delay scan. The horizontal x-axis represents the 1280 strip channels, the vertical y-axis corresponds to the delay in 10 ns steps, and the color scale indicates the pedestal-corrected output from Gotthard-II. The laser was injected into the strip channels around channel 900. The right side of the figure shows the projection of the image onto the y-axis, representing the sum of the detector's output across all strip channels, after pedestal correction, as a function of the delay. The measured Full Width at Half Maximum (FWHM) of the exposure window is measured at 110 ns (marked in black), consistent with the design. The width of the exposure window with complete signal collection is 80 ns, which is suitable for measuring single X-ray bunches at FELs or isolated Camshaft X-ray bunches at synchrotrons. The falling edge of the delay scan reveals a signal settling time of 40-50 ns in Gotthard-II.

After the scan, the delay for triggering the infrared laser was set to 100 ns, ensuring that the laser arrived in the middle of the exposure window with all signals fully settled in the detector. In this configuration, 10,000 frames were taken with Gotthard-II at a 400 kHz frame rate, using the infrared laser at the same repetition rate (2.5 μs period). Since the infrared laser is reliably triggered by the external signal, if the detector is unable to capture images at the same rate, certain frames would miss the laser signal and display empty frames. Figure 23b shows the pedestal-corrected output of the 1280 strip channels of Gotthard-II across all 10,000 frames. The injected strip channel (around channel 900) consistently shows the correct output. The inset in Figure 23b highlights the output for 40 consecutive frames (100 μs) in the zoomed region. The laboratory-based laser measurement demonstrates the capability of Gotthard-II to perform continuous imaging at 400 kHz, the expected signal rise time, and the capability to synchronize to XFEL pulses or isolated pulses at synchrotrons.

5. CONCLUSIONS

The Gotthard-II detector, developed at PSI with two different strip pitches of 50 and 25 μm, demonstrates single-photon sensitivity for hard X-rays down to 5.4 keV with a signal-to-noise ratio greater than 5, and a large dynamic range exceeding 10^5 keV, based on its dynamic gain switching architecture. With an on-chip analog-to-digital converter and local digital storage, it is capable of capturing images at a 4.5 MHz frame rate, recording all 2700 pulses produced by the EuXFEL. This allows Gotthard-II to fully utilize the capabilities of the FEL machine, something not achievable by the other detectors currently installed and operational at the facility. Additionally, its continuous imaging capability at up to 400 kHz frame rate makes Gotthard-II applicable for experiments at synchrotron radiation sources and future FEL facilities operating in continuous wave (CW) mode with high repetition rates.

In this paper, we have introduced the design of the Gotthard-II detector, discussed the calibration procedure for the on-chip ADC, and the conversion gains and offsets across the full dynamic range. We have also validated the detector's usability in several experiments and compared the results with those obtained from other established detectors at the beamline. Over 30 Gotthard-II detectors have been commissioned at the EuXFEL,[35] and we look forward to exploring the full potential of Gotthard-II in user experiments.

The future work includes the improvements of the ADC with higher resolution, removal of the oversized digital memory, and implementation of a high-speed serial link of >3 Gbps in the ASIC, which will enable a full >4.5 MHz continuous frame rate CW detector.

■ ASSOCIATED CONTENT

Data Availability Statement

Experimental data for lab tests and from beam tests at the SLS are stored on the server of the Paul Scherrer Institute; data of the XES measurements performed at the EuXFEL are stored at the server of the EuXFEL. They can be made available and accessible upon reasonable requests.

■ AUTHOR INFORMATION

Corresponding Author

Jiaguo Zhang − *Paul Scherrer Institut, 5232 Villigen-PSI, Switzerland;* orcid.org/0000-0001-7446-210X; Email: jiaguo.zhang@psi.ch

Authors

Anna Bergamaschi − *Paul Scherrer Institut, 5232 Villigen-PSI, Switzerland*

Martin Brückner − *Paul Scherrer Institut, 5232 Villigen-PSI, Switzerland*

Maria Carulla − *Paul Scherrer Institut, 5232 Villigen-PSI, Switzerland*

Roberto Dinapoli − *Paul Scherrer Institut, 5232 Villigen-PSI, Switzerland*

Simon Ebner − *Paul Scherrer Institut, 5232 Villigen-PSI, Switzerland*

Khalil Daniel Ferjaoui − *Paul Scherrer Institut, 5232 Villigen-PSI, Switzerland*

Erik Fröjdh − *Paul Scherrer Institut, 5232 Villigen-PSI, Switzerland*

Viveka Gautam − *Paul Scherrer Institut, 5232 Villigen-PSI, Switzerland*

Dominic Greiffenberg − *Paul Scherrer Institut, 5232 Villigen-PSI, Switzerland*

Vadym Kedych − *Paul Scherrer Institut, 5232 Villigen-PSI, Switzerland*

Dmitry Khakhulin − *European XFEL, 22869 Schenefeld, Germany*

Shqipe Hasanaj − *Paul Scherrer Institut, 5232 Villigen-PSI, Switzerland*

Julian Heymes − *Paul Scherrer Institut, 5232 Villigen-PSI, Switzerland*

https://doi.org/10.1021/photonsci.5c00027
Photon Sci. XXXX, XXX, XXX−XXX

Viktoria Hinger − *Paul Scherrer Institut, 5232 Villigen-PSI, Switzerland*
Thomas King − *Paul Scherrer Institut, 5232 Villigen-PSI, Switzerland*
Shuqi Li − *Paul Scherrer Institut, 5232 Villigen-PSI, Switzerland*
Carlos Lopez-Cuenca − *Paul Scherrer Institut, 5232 Villigen-PSI, Switzerland*
Alice Francesca Mazzoleni − *Paul Scherrer Institut, 5232 Villigen-PSI, Switzerland*
Davide Mezza − *Paul Scherrer Institut, 5232 Villigen-PSI, Switzerland*
Konstantinos Moustakas − *Paul Scherrer Institut, 5232 Villigen-PSI, Switzerland*
Martin Müller − *Paul Scherrer Institut, 5232 Villigen-PSI, Switzerland*
Jonathan Franklin Mulvey − *Paul Scherrer Institut, 5232 Villigen-PSI, Switzerland*
Aldo Mozzanica − *Paul Scherrer Institut, 5232 Villigen-PSI, Switzerland*
Kirsty Anne Paton − *Paul Scherrer Institut, 5232 Villigen-PSI, Switzerland*
Marco Ramilli − *European XFEL, 22869 Schenefeld, Germany*
Christian Ruder − *Paul Scherrer Institut, 5232 Villigen-PSI, Switzerland*
Patrick Sieberer − *Paul Scherrer Institut, 5232 Villigen-PSI, Switzerland;* orcid.org/0000-0002-9616-2244
Saverio Silletta − *Paul Scherrer Institut, 5232 Villigen-PSI, Switzerland*
Bernd Schmitt − *Paul Scherrer Institut, 5232 Villigen-PSI, Switzerland*
Grigory Smolentsev − *Paul Scherrer Institut, 5232 Villigen-PSI, Switzerland;* orcid.org/0000-0001-7348-7276
Dhanya Thattil − *Paul Scherrer Institut, 5232 Villigen-PSI, Switzerland*
Monica Turcato − *European XFEL, 22869 Schenefeld, Germany*
Xiangyu Xie − *Paul Scherrer Institut, 5232 Villigen-PSI, Switzerland*
Hazem Yousef − *European XFEL, 22869 Schenefeld, Germany*

Complete contact information is available at: https://pubs.acs.org/10.1021/photonsci.5c00027

Notes

The authors declare no competing financial interest.

■ ACKNOWLEDGMENTS

The authors would like to thank Dr. Nicola Pietro Maria Casati (PSI) for the support of the XRD measurements at the MS beamline of the SLS. Kirsty A. Paton has received funding from MSCA PSI-FELLOW-3i (EU grant agreement No. 884104). We acknowledge European XFEL in Schenefeld, Germany, for provision of X-ray free electron laser beamtime (proposal Nr 3225, 10.22003/XFEL.EU-DATA-003225-00) at the FXE instrument and thank the instrument group and facility staff for their assistance.

■ REFERENCES

(1) Decking, W.; Abeghyan, S.; Abramian, P.; Abramsky, A.; Aguirre, A.; Albrecht, C.; Alou, P.; Altarelli, M. A MHz-repetition-rate hard X-ray free-electron laser driven by a superconducting linear accelerator. *Nat. Photonics* **2020**, *14*, 0607.
(2) Allahgholi, A.; Becker, J.; Delfs, A.; Dinapoli, R.; Goettlicher, P.; Greiffenberg, D.; Henrich, B.; Hirsemann, H.; Kuhn, M.; Klanner, R.; Klyuev, A.; Krueger, H.; Lange, S.; Laurus, T.; Marras, A.; Mezza, D.; Mozzanica, A.; Niemann, M.; Poehlsen, J.; Schwandt, J.; Sheviakov, I.; Shi, X.; Smoljanin, S.; Steffen, L.; Sztuk-Dambietz, J.; Trunk, U.; Xia, Q.; Zeribi, M.; Zhang, J.; Zimmer, M.; Schmitt, B.; Graafsma, H. The adaptive gain integrating pixel detector at the European XFEL. *J. Synchrotron Rad.* **2019**, *26*, 74−82.
(3) Hart, M.; Angelsen, C.; Burge, S.; Coughlan, J.; Halsall, R.; Koch, A.; Kuster, M.; Nicholls, T.; Prydderch, M.; Seller, P.; Thomas, S.; Blue, A.; Joy, A.; O'Shea, V.; Wing, M.Development of the LPD, a high dynamic range pixel detector for the European XFEL. In *2012 IEEE Nuclear Science Symposium and Medical Imaging Conference Record (NSS/MIC)*; IEEE, 2012; pp 534−537 .
(4) Porro, M.; Andricek, L.; Aschauer, S.; Castoldi, A.; Donato, M.; Engelke, J.; Erdinger, F.; Fiorini, C.; Fischer, P.; Graafsma, H.; Grande, A.; Guazzoni, C.; Hansen, K.; Hauf, S.; Kalavakuru, P.; Klaer, H.; Tangl, M.; Kugel, A.; Kuster, M.; Lechner, P.; Lomidze, D.; Maffessanti, S.; Manghisoni, M.; Nidhi, S.; Okrent, F.; Re, V.; Reckleben, C.; Riceputi, E.; Richter, R.; Samartsev, A.; Schlee, S.; Soldat, J.; Strüder, L.; Szymanski, J.; Turcato, M.; Weidenspointner, G.; Wunderer, C. B. The MiniSDD-Based 1-Mpixel Camera of the DSSC Project for the European XFEL. *IEEE Trans. Nucl. Sci.* **2021**, *68*, 1334−1350.
(5) Mozzanica, A.; Andrä, M.; Barten, R.; Bergamaschi, A.; Chiriotti, S.; Brückner, M.; Dinapoli, R.; Fröjdh, E.; Greiffenberg, D.; Leonarski, F.; Lopez-Cuenca, C.; Mezza, D.; Redford, S.; Ruder, C.; Schmitt, B.; Shi, X.; Thattil, D.; Tinti, G.; Vetter, S.; Zhang, J. The JUNGFRAU Detector for Applications at Synchrotron Light Sources and XFELs. *Synchrotron Radiat. News* **2018**, *31*, 16−20.
(6) Wiedorn, M. O.; Oberthür, D.; Bean, R.; Schubert, R.; Werner, N.; Abbey, B.; Aepfelbacher, M.; Adriano, L. Megahertz serial crystallography. *Nat. Commun.* **2018**, *9*, No. 4025.
(7) Kirkwood, H. J.; Wijn, R.; Mills, G.; Letrun, R.; Kloos, M.; Vakili, M.; Karnevskiy, M. A multi-million image Serial Femtosecond Crystallography dataset collected at the European XFEL. *Sci. Data* **2022**, *9*, No. 161.
(8) Kujala, N.; Freund, W.; Liu, J.; Koch, A.; Falk, T.; Planas, M.; Dietrich, F.; Laksman, J.; Maltezopoulos, T.; Risch, J.; Dall'Antonia, F.; Gruenert, J. Hard x-ray single-shot spectrometer at the European X-ray Free-Electron Laser. *Rev. Sci. Instrum.* **2020**, *91*, No. 103101.
(9) Zhang, J.; Andrä, M.; Barten, R.; Bergamaschi, A.; Brückner, M.; Dinapoli, R.; Fröjdh, E.; Greiffenberg, D.; Lopez-Cuenca, C.; Mezza, D.; Mozzanica, A.; Ramilli, M.; Redford, S.; Ruat, M.; Ruder, C.; Schmitt, B.; Shi, X.; Thattil, D.; Tinti, G.; Turcato, M.; Vetter, S. Towards Gotthard-II: development of a silicon microstrip detector for the European X-ray Free-Electron Laser. *J. Instrum.* **2018**, *13*, No. P01025.
(10) Zhang, J.; Andrä, M.; Barten, R.; Bergamaschi, A.; Brückner, M.; Dinapoli, R.; Fröjdh, E.; Greiffenberg, D.; Lopez-Cuenca, C.; Mezza, D.; Mozzanica, A.; Ramilli, M.; Redford, S.; Ruat, M.; Ruder, C.; Schmitt, B.; Shi, X.; Thattil, D.; Tinti, G.; Turcato, M.; Vetter, S. Performance evaluation of the analogue front-end and ADC prototypes for the Gotthard-II development. *J. Instrum.* **2017**, *12*, No. C12052.
(11) Zhang, J.; Andrä, M.; Barten, R.; Bergamaschi, A.; Brückner, M.; Chiriotti-Alvarez, S.; Dinapoli, R.; Fröjdh, E.; Greiffenberg, D.; Kozlowski, P.; Kuster, M.; Lopez-Cuenca, C.; Meyer, M.; Mezza, D.; Mozzanica, A.; Ramilli, M.; Ruder, C.; Schmitt, B.; Shi, X.; Thattil, D.; Tinti, G.; Turcato, M.; Vetter, S. Design and first tests of the Gotthard-II readout ASIC for the European X-ray Free-Electron Laser. *J. Instrum.* **2021**, *16*, No. P04015.
(12) Hamamatsu Photonics website: https://www.hamamatsu.com/eu/en.html.
(13) Intel Cyclone 10GX website: https://www.intel.com/content/www/us/en/products/details/fpga/cyclone/10/gx.html.

https://doi.org/10.1021/photonsci.5c00027
Photon Sci. XXXX, XXX, XXX−XXX

(14) Nios II soft-core processor website: https://www.intel.com/content/www/us/en/docs/programmable/683620/current/processor-system-basics.html).
(15) Redford, S.; Bergamaschi, A.; Brückner, M.; Cartier, S.; Dinapoli, R.; Ekinci, Y.; Fröjdh, E.; Greiffenberg, D.; Mayilyan, D.; Mezza, D.; Mozzanica, A.; Rajeev, R.; Ramilli, M.; Ruder, C.; Schädler, L.; Schmitt, B.; Shi, X.; Thattil, D.; Tinti, G.; Zhang, J. Calibration status and plans for the charge integrating JUNGFRAU pixel detector for SwissFEL. *J. Instrum.* **2016**, *11* (11), No. C11013.
(16) Redford, S.; Andrä, M.; Barten, R.; Bergamaschi, A.; Brückner, M.; Dinapoli, R.; Fröjdh, E.; Greiffenberg, D.; Lopez-Cuenca, C.; Mezza, D.; Mozzanica, A.; Ramilli, M.; Ruat, M.; Ruder, C.; Schmitt, B.; Shi, X.; Thattil, D.; Tinti, G.; Vetter, S.; Zhang, J. First full dynamic range calibration of the JUNGFRAU photon detector. *J. Instrum.* **2018**, *13* (01), No. C01027.
(17) Sikorski, M.; Ramilli, M.; de Wijn, R.; Hinger, V.; Mozzanica, A.; Schmitt, B.; Han, H.; Bean, R.; Bielecki, J.; Bortel, G.; Dietze, T.; Faigel, G.; Kharitonov, K.; Kim, C.; Koliyadu, J. C. P.; Koua, F. H. M.; Letrun, R.; Lopez, L. M.; Reimers, N.; Round, A.; Sarma, A.; Sato, T.; Tegze, M.; Turcato, M. First operation of the JUNGFRAU detector in 16-memory cell mode at European XFEL. *Front. Phys.* **2023**, *11*, No. 1303247.
(18) Sztuk-Dambietz, J.; Rovensky, V.; Klujev, A.; Laurus, T.; Trunk, U.; Ahmed, K.; Meyer, O.; Möller, J.; Parenti, A.; Raab, N.; Shayduk, R.; Sikorski, M.; Ansaldi, G.; Bösenberg, U.; Lopez, L. M.; Muenich, A.; Preston, T. R.; Schmidt, P.; Stern, S.; Bean, R.; Madsen, A.; Gelisio, L.; Hauf, S.; Gessler, P.; Wrona, K.; Graafsma, H.; Turcato, M. Operational experience with Adaptive Gain Integrating Pixel Detectors at European XFEL. *Front. Phys.* **2024**, *11*, No. 1329378.
(19) Mezza, D.; Allahgholi, A.; Delfs, A.; Dinapoli, R.; Goettlicher, P.; Graafsma, H.; Greiffenberg, D.; Hirsemann, H.; Klyuev, A.; Laurus, T.; Marras, A.; Mozzanica, A.; Perova, I.; Poehlsen, J.; Schmitt, B.; Sheviakov, I.; Shi, X.; Trunk, U.; Xia, Q.; Zhang, J.; Zimmer, M. New calibration circuitry and concept for AGIPD. *J. Instrum.* **2016**, *11*, No. C11019.
(20) Mezza, D.; Becker, J.; Carraresi, L.; Castoldi, A.; Dinapoli, R.; Goettlicher, P.; Graafsma, H.; Greiffenberg, D.; Hirsemann, H.; Klujev, A.; Kuhn, M.; Lange, S.; Laurus, T.; Maffessanti, S.; Marras, A.; Mozzanica, A.; Poehlsen, J.; Redford, S.; Ruder, C.; Schmitt, B.; Sheviakov, I.; Shi, X.; Trunk, U.; Vetter, S.; Zhang, J.; Zimmer, M. Calibration methods for charge integrating detectors. *Nucl. Instrum. Methods Phys. Res., Sect. A* **2022**, *1024*, No. 166078.
(21) Moll, M. PhD thesis (1999): DESY-THESIS-1999-040. https://bib-pubdb1.desy.de/record/300958.
(22) Bergamaschi, A.; Cervellino, A.; Dinapoli, R.; Gozzo, F.; Henrich, B.; Johnson, I.; Kraft, P.; Mozzanica, A.; Schmitt, B.; Shi, X. The MYTHEN detector for X-ray powder diffraction experiments at the Swiss Light Source. *J. Synchrotron Radiat.* **2010**, *17* (5), 653−668.
(23) Bergamaschi, A.; Andrä, M.; Barten, R.; Baruffaldi, F.; Brückner, M.; Carulla, M.; Chiriotti, S.; Dinapoli, R.; Fröjdh, E.; Greiffenberg, D.; Hasanaj, S.; Heymes, J.; Hinger, V.; Kozlowski, P.; Lopez-Cuenca, C.; Mezza, D.; Mozzanica, A.; Moustakas, K.; Ruder, C.; Schmitt, B.; Thattil, D.; Zhang, J. First demonstration of on-chip interpolation using a single photon counting microstrip detector. *Journal of Instrumentation* **2022**, *17* (11), No. C11012.
(24) Andrä, M.; Dinapoli, R.; Bergamaschi, A.; Barten, R.; Brückner, M.; Chiriotti Alvarez, S.; Fröjdh, E.; Greiffenberg, D.; Lopez-Cuenca, C.; Mezza, D.; Mozzanica, A.; Redford, S.; Ruder, C.; Schmitt, B.; Shi, X.; Thattil, D.; Tinti, G.; Vetter, S.; Zhang, J. Towards MYTHEN 3: Characterization of prototype chips. *Nucl. Instrum. Methods Phys. Res., Sect. A* **2019**, *936*, 383−385.
(25) Andrä, M. PhD thesis at ETH Zurich, 2021 DOI: 10.3929/ethz-b-000462676.
(26) Andrä, M.; Bergamaschi, A.; Baruffaldi, F.; Brückner, M.; Carulla, M.; Casati, N.; Cervellino, A.; Dinapoli, R.; Fröjdh, E.; Greiffenberg, D.; Hasanaj, S.; Heymes, J.; Hinger, V.; Kozlowski, P.; Lopez Cuenca, C.; Meister, D.; Mezza, D.; Moustakas, K.; Mozzanica, A.; Paton, K.; Ruder, C.; Scagnoli, V.; Smolentsev, G.; Schmitt, B.; Thattil, D.; Xie, X.; Zhang, J. MYTHEN III: advancements in single photon counting detectors for synchrotron powder diffraction experiments. *J. Synchrotron Radiat.* **2025**, *32* (2), 365−377.
(27) Vankó, G.; Glatzel, P.; Pham, V.−T.; Abela, R.; Grolimund, D.; Borca, C. N.; Johnson, S. L.; Milne, C. J.; Bressler, C. Picosecond time-resolved X-ray emission spectroscopy: ultrafast spin-state determination in an iron complex. *Angew. Chem., Int. Ed.* **2010**, *49* (34), 5910−5912.
(28) Vankó, G.; Bordage, A.; Glatzel, P.; Gallo, E.; Rovezzi, M.; Gawelda, W.; Galler, A.; Bressler, C.; Doumy, G.; March, A. M.; Kanter, E. P.; Young, L.; Southworth, S. H.; Canton, S. E.; Uhlig, J.; Smolentsev, G.; Sundström, V.; Haldrup, K.; Brandt van Driel, T.; Nielsen, M. M.; Kjaer, K. S.; Lemke, H. T. Spin-state studies with XES and RIXS: From static to ultrafast. *J. Electron Spectrosc. Relat. Phenom.* **2013**, *188*, 166−171.
(29) Zhang, W.; Alonso-Mori, R.; Bergmann, U.; et al. Tracking excited-state charge and spin dynamics in iron coordination complexes. *Nature* **2014**, *509* (7500), 345−348.
(30) March, A. M.; Assefa, T. A.; Boemer, C.; Bressler, C.; Britz, A.; Diez, M.; Doumy, G.; Galler, A.; Harder, M.; Khakhulin, D.; et al. Probing transient valence orbital changes with picosecond valence-to-core X-ray emission spectroscopy. *J. Phys. Chem. C* **2017**, *121* (5), 2620−2626.
(31) Alonso-Mori, R.; Sokaras, D.; Cammarata, M.; Ding, Y.; Feng, Y.; Fritz, D.; Gaffney, K. J.; Hastings, J.; Kao, C.-C.; Lemke, H. T.; Maxwell, T.; Robert, A.; Schropp, A.; Seiboth, F.; Sikorski, M.; Song, S.; Weng, T.-C.; Zhang, W.; Glenzer, S.; Bergmann, U.; Zhu, D. Femtosecond electronic structure response to high intensity XFEL pulses probed by iron X-ray emission spectroscopy. *Sci. Rep.* **2020**, *10* (1), No. 16837.
(32) Galler, A.; Gawelda, W.; Biednov, M.; Bömer, C.; Britz, A.; Brockhauser, S.; Choi, T.-K.; Diez, M.; Frankenberger, P.; French, M.; Görries, D.; Hart, M.; Hauf, S.; Khakhulin, D.; Knoll, M.; Korsch, T.; Kubicek, K.; Kuster, M.; Lang, P.; Alves Lima, F.; Otte, F.; Schulz, S.; Zalden, P.; Bressler, C. Scientific instrument Femtosecond X-ray Experiments (FXE): instrumentation and baseline experimental capabilities. *J. Synchrotron Radiat.* **2019**, *26* (5), 1432−1447.
(33) Khakhulin, D.; Otte, F.; Biednov, M.; Bömer, C.; Choi, T.-K.; Diez, M.; Galler, A.; Jiang, Y.; Kubicek, K.; Lima, F. A.; Rodriguez-Fernandez, A.; Zalden, P.; Gawelda, W.; Bressler, C. Ultrafast X-ray photochemistry at European XFEL: Capabilities of the Femtosecond X-ray Experiments (FXE) instrument. *Appl. Sci.* **2020**, *10* (3), 995.
(34) Lima, F. A.; Otte, F.; Vakili, M.; Ardana-Lamas, F.; Biednov, M.; Dall'Antonia, F.; Frankenberger, P.; Gawelda, W.; Gelisio, L.; Han, H.; Jiang, Y.; Kloos, M.; Kluyver, T.; Knoll, M.; Kubicek, K.; Bermudez Macias, I. J.; Schulz, J.; Turkot, O.; Uemura, Y.; Valerio, J.; Yousef, H.; Zalden, P.; Khakhulin, D.; Bressler, C.; Milne, C.; et al. Experimental capabilities for liquid jet samples at sub-MHz rates at the FXE Instrument at European XFEL. *J. Synchrotron Radiat.* **2023**, *30* (6), 1168−1182.
(35) Ramilli, M.; Ahmed, K.; de Wijn, R.; Dietze, T.; Fernandes, B.; Hammer, D.; Jiang, Y.; Khakhulin, D.; Koliyadu, J. C. P.; Letrun, R.; Liu, J.; Lopez-Cuenca, C.; Mezza, D.; Milne, C.; Mozzanica, A.; Parenti, A.; Sato, T.; Schmidt, P.; Schmitt, B.; Sikorski, M.; Turcato, M.; Uemura, Y.; Wang, H.; Yousef, H.; Zhang, J. Integration and first operation of the Gotthard-II detector at European XFEL. *Nucl. Instrum. Methods Phys. Res., Sect. A* **2024**, *1058*, No. 168796.

https://doi.org/10.1021/photonsci.5c00027
Photon Sci. XXXX, XXX, XXX−XXX